VOLUME 7 NUMBER 3-4 2020 ISSN 2409-6121; eISSN 2522-1361

Physical Sciences and Technology

National Nanotechnological Laboratory of Open Type
Institute of Experimental and Theoretical Physics

Physical Sciences and Technology is publishing two number in a year by al-Farabi Kazakh National University, al-Farabi ave., 71, 050040, Almaty, the Republic of Kazakhstan
website: http://phst.kaznu.kz/

Any inquiry for subscriptions should be send to:
Gauhar Mussabek, al-Farabi Kazakh National University
al-Farabi ave., 71, 050040, Almaty, the Republic of Kazakhstan
e-mail: gauharmussabek@gmail.com

SCOPE AND AIM

Physical Sciences and Technology provides an original paperback for the publication of peerreviewed research and review articles in all fields of Physics and related Technology. The topics, included in the scope, especially emphasize understanding of the physics underlying modern technology.

Subject areas may include, but are not limited to the following fields: Astronomy and Space Research, Theoretical Physics and Astrophysics, Plasma Physics and Related Technology, Chemical Physics and Related Technology, Condensed Matter Physics and Related Technology, Thermal physics and Related Technology, Nuclear Physics and Related Technology, Nanomaterials and Nanotechnology, Applied Atomic and Molecular Physics, Material Sciences and Related Technology, Electronics and Related Technology, Instrumentation, Photonics and Quantum Electronics, Signal processing.

The Journal is issued under the auspices of the National Nanotechnological Laboratory of Open Type and Institute of Experimental and Theoretical Physics and is published two times a year by the «Kazakh University» Publishing House. The International Editorial Board of the Journal consists of leading researchers from different countries of the world. The Journal is wide open for contributions that both lie at the far frontiers of contemporary physics and are particularly aimed at applications of the scientific principles of physics to modern technological problems.

IRSTI 29.27.07 https://doi.org/10.26577/phst.2020.v7.i2.01

Dust particles influence on a stratified glow discharge

A. Fedoseev* and N. Demin

Institute of Thermophysics SB RAS, 1, Lavrentyev Ave., 630090, Novosibirsk, Russia
**e-mail: fedoseev@itp.nsc.ru*

In this work, the correlations between the parameters of a DC glow discharge and dust particles in a low-temperature plasma have been studied. The formation of voids inside the dust cloud was studied, depending on the characteristics of the discharge (the discharge pressure, type of gas and discharge current) and dust particles (their quantity and size). We have demonstrated that the ion drag force could lead to the formation of voids in the center of the cloud of dust grains, which levitate in the field of a stratified positive column. It has also been demonstrated that the accumulation of dust particles affects the discharge plasma in a non-local way, i.e., the density distribution of dust grains and the charge of each individual particle depend on the plasma parameters outside the dust cloud. The presented qualitative estimates are important for understanding the processes occurring in complex plasma of a glow discharge.

Key words: dusty plasma, stratified glow discharge, voids in dusty plasma, Boltzmann equation for electron distribution function, Havnes parameter.
PACS numbers: 52.20.−j, 52.27.Lw.

1 Introduction

Dusty plasma is a complex medium that includes ionized gas and micron-sized solid particles that acquire a significant charge in this gas [1-3]. Such an environment can most often be found in outer space, but it is also common in industry (for example, in chemical deposition and coating processes). In laboratory conditions, dusty plasma is studied in the RF [4, 5] and in DC glow discharges [6-8]. There are also studies of dust particles in combined discharges of RF + DC [9-10]. As a result of extensive research, many interesting phenomena were discovered and studied in a dusty plasma, such as the ordering of dust particles into structures, phase transitions between different types of ordered structures, the formation of vortices in a dusty plasma, the propagation of sound waves, etc. [1-3].

The phenomenon of the appearance of large voids in a dust cloud under microgravity conditions in RF discharges is a well-known [11-12]. Various analytical models have been developed for its description [13-15]. Because of experimental, theoretical and numerical studies, it was found that the ion drag force, which arises due to the outflow of ions from the ionization source, is responsible for the formation of voids in the dust cloud [13].

In a dusty plasma obtained in laboratory conditions (both in direct current discharges and radio frequency discharges), the density of ions and electrons is $n_i \approx n_e \sim 10^7$-$10^9$ cm^{-3}, the density of dust particles is $N_d \sim 10^2$-10^8 cm^{-3}, the charge of each dust particle can vary in the range $eZ_d = (10^3\text{-}10^5)\ e$. In the case when the Havnes parameter $P_H = Z_d\ N_d/n_e << 1$, the charge of dust grains is determined from the conditions in the plasma. At large P_H, local plasma distributions near dust particles (electron density, electric potential distribution, electron energy distribution function (EEDF)) change, which causes the average charge of charge of dust grains. The non-local effect of dust particles on the properties of a RF discharge, which is widely used in the semiconductor industry, was studied using particles in a cell method by J. P. Boeuf [16]. As a result of research, it was found that each dust particle is a sink for ions and electrons, which means that a cloud of high-density dust particles will have a significant effect on the properties of the plasma and the conditions of confinement of the dust grains themselves. However, this important phenomenon is often omitted in studies of dusty plasma in discharges. Moreover, so far in many works it is often assumed that the electron energy distribution function is Maxwellian.

At present day, a significant number of works have been published that are devoted to how dust grains affect plasma characteristics [16–28]. As a result of these studies, it was concluded that the loss of electrons and ions due to dust particles is compensated by ionizing collisions, therefore in the region containing dust particles, the averaged electric field increases. In [17–18], a self-consistent kinetic model was used, which showed that an increase in the concentration of dust grains leads to an increase in the ion density and an averaged electric field, as well as to a decrease in the electron density and the average charge of the dust particles of the cloud. However, it is worth noting that the number of dust particles in this model was set, and the effect of dust particles on the plasma was taken into account in the local approach.

In the case when the density of dust particles in the cloud is very high, its effect on the distribution in the discharge plasma becomes non-local [21-23]. One of the important consequences of this non-locality is that the average charge of particle grains depends on the fluxes of ions and electrons into the cloud from the plasma outside the cloud. In many articles, the characteristics of dust particles are studied without taking into account their influence on the parameters of a gas-discharge plasma. For example, the electric field that holds dust particles is usually considered constant and is specified as a parameter. The influence of a dust cloud on radial distributions in plasma was studied by a nonlocal kinetic model in [24–28]. The purpose of this work is to emphasize the non-local effect of dust particle accumulation on DC discharge plasma.

2 Kinetic approach for description of dusty plasma parameters

Based on the Boltzmann equation for EEDF, a self-consistent kinetic study of the influence of the density of dust particles N_d on the PC parameters of a low-pressure direct current glow discharge for a noble gas plasma was carried out. It should be noted that even without dust grains, a glow discharge in cylindrical tubes is a very complex non-equilibrium system of ions, electrons, and neutral atoms. At some initial parameters, the glow discharge self-organizes (stratification of the positive column), and nonlocal processes play an important role in this. The addition of dust particles to this complex system substantially complicates its description. A simplified model is considered here, which is able to isolate the main problems of the interaction of dust grain clusters and plasma parameters.

The charge of each specific dust particle is found from the OML approximation, that is, in the case in which the average mean free path of ions l_i in the plasma significantly exceeds both the dust grain size r_0 and the screening length λ_i. This work does not take into account the capture of ions by dust grain and, as a consequence of this, the occurrence of an additional collisional ion flux. In [29, 30], it was found that the capture of ions by a dust particle leads to screening of the charge of the dust particle and to a decrease in its charge. Nevertheless, this does not change the qualitative conclusions about the effect of the density of dust particles on the discharge parameters. It is also worth considering the non-Maxwellian character of EEDF in a non-equilibrium low-temperature dusty plasma.

In order to describe the formation of voids in dust clouds in a direct current discharge, a previously developed self-consistent kinetic model was used to calculate the radial distributions of dust plasma parameters [22-23]. In this model, it was assumed that a cloud of dusty spherical grains of radius $r_0 \sim 1$ μm has a certain distribution of radial density $N_d(r)$. The Boltzmann equation for the electron energy distribution function was used in the “two-term” approximation for the isotropic f_0:

$$\sqrt{\frac{m_e\varepsilon}{2}}\frac{\partial f_0}{\partial t}=\frac{1}{r}\frac{\partial}{\partial r}\left[\frac{r\varepsilon}{3H}\left(\frac{\partial f_0}{\partial r}-e_0E_z\frac{\partial f_0}{\partial \varepsilon}\right)\right]+\frac{\partial}{\partial \varepsilon}\left[\frac{\varepsilon}{3H}\left(-e_0E_r\frac{\partial f_0}{\partial r}+e_0^2\left(E_r^2+E_z^2\right)\frac{\partial f_0}{\partial \varepsilon}\right)\right]+ \tag{1}$$

$$+\frac{\partial}{\partial \varepsilon}\left[C(\varepsilon)f_0\right]-G(\varepsilon)f_0+S(f_0)+S_{ion}(f_0)+S_d(f_0),$$

and anisotropic (axial f_z and radial f_r) components related, respectively, to the similar components of the electric field, $E_r(r)$ and $E_z(r)$. Coefficients C, G, and S determine the energy lost in elastic and inelastic collisions. The value of E_z was calculated from the balance of the formation of ions and electrons as a result of ionization $S_{ion}(f_0)$ and their recombination on the surface of dust particles and on the walls of the discharge tube. Obviously, these processes are non-local. The radial j_{er} and axial j_{ez} current densities, electron density $n_e(r)$, ionization rate constants, and electron and ion absorption rates on the surface of dust particles were calculated from the Boltzmann equation. To calculate the ion density $n_i(r)$, the drift-diffusion equation is used with the conditions for their loss upon absorption on the surface of dust particles and the formation of ions in electron-atom collisions:

$$\frac{\partial n_i(r,t)}{\partial t} - \frac{1}{r}\frac{\partial}{\partial r} r\left(\mu_i n_i(r,t) E_r(r,t) - D_i \frac{\partial n_i(r,t)}{\partial r} \right) = \nu_{io}(r,t) - \nu_{rec}(r,t), \quad (2)$$

In the absence of dust particles, in noble gases, the diffusion coefficients D_i and ion drift μ_i are determined only by charge exchange collisions and are related to each other by the Einstein relation. In the discharge where dust grains are located, the drift and diffusion coefficients depend both on the density of dust particles $N_d(r)$ and on the gas density N_g.

The density of dust particles $N_d(r)$ was calculated by the drift diffusion equation:

$$\frac{\partial n_d(r,t)}{\partial t} - \frac{1}{r}\frac{\partial}{\partial r} r\left(\mu_d n_d(r,t) F_d(r,t) - D_d \frac{\partial n_d(r,t)}{\partial r} \right) = 0. \quad (3)$$

It was assumed that the diffusion coefficients D_d and mobility μ_d of dust particles obey the Einstein relation. In this work, temperature T_d = 10 eV is used, due to the fact that the temperature of dust particles was not so significant for the results obtained. Dust grains are confined in the center of the tube and form a dust cloud. Due to the lack of sources of dust particles losses, we do not need to take the actual values of the mobility and diffusion coefficients only taking into account the Einstein relation between them. In the process of numerical calculation, the radial profile of the dust density is estimated, and in the final state, the radial flux of dust particles $j_{dr}(r) = 0$. The total force F_{tot}, which affects the dust grain in the radial direction, is determined by the superposition of forces:

$$F_{tot} = F_E + F_{id} + F_{th} + F_{dd}, \quad (4)$$

where $F_E = -eZ_d(r)E_r(r)$ is electric force, $F_{id} \sim j_{ir}(r)$ is the ion drag force, F_{dd} is the repulsion forces of dust particles (calculated similarly to [22]), and $F_{th} \sim \Delta T$ is the thermophoretic force. The forces F_{id} and F_{th} are opposite in direction to F_E, which leads to the formation of voids in the central part of the dust cloud in the middle of the discharge tube under certain conditions. There are many works that are devoted to assessing the strength of ion drag force. In this work, F_{id} was taken as in [22]:

$$F_{id} = \frac{\sqrt{8\pi}}{3} n_i u_i v_{T_i} R_C^2 m_i \left[\Lambda(\beta_T) + \sqrt{\frac{2}{\pi}} \kappa\left(\frac{\lambda_D}{l_i} \right) \right]. \quad (5)$$

Here $\Lambda(\beta_T)$ is the modified Coulumb logarithm and $\kappa(x)$ – a collisional function, the exact expressions are given in [22].

The equations for ions, electrons, and dust particles were supplemented by the Poisson equation, which calculated the self-consistent electric field $E_r(r)$:

$$\frac{1}{r}\frac{\partial(rE_r(r,t))}{\partial r} = 4\pi e_0 \left[n_i(r,t) - n_e(r,t) \right]. \quad (6)$$

Thus, a complete system of equations is obtained for the self-consistent determination of $n_e(r)$, $n_i(r)$, $N_d(r)$ и $E_r(r)$. In this paper, we solved the

non-stationary case for ions, electrons, and dust particles based on the balance equations obtained using the Boltzmann equation for EEDF and the electric field obtained from the Poisson equation. At each time step, the charge number Z_d was determined from the condition of the balance of fluxes of ions and electrons on the surface of the dust grain ($I_e + I_i = 0$), taking into account the distribution functions of ions and electrons [22]. The axial electric field voltage was recounted at each time step using the feedback between the discharge current E_z and I_d. The procedure was repeated until the parameters of dust particles and plasma distributions completely converged. It is worth noting that the evolution of plasma parameters in time has not been considered here, since only the final convergent solution for the given parameters of the gas discharge is of interest.

3 Results and discussion

In the present work, we study a stratified positive column of a glow discharge in a quasi-2D arrangement. In the absence of dust grains in the tube, the axial electric field is E_z, and the electron current density on the tube axis is j_z. In the stationary state, the creation of new ions and electrons is completely compensated by their recombination on the tube wall, which is determined by the process of ambipolar diffusion. It is known that EEDF depends only on parameter E_z/N_g. If, however, micron-sized dust particles with a density of N_d are placed in the discharge, then ions and electrons will participate in the recombination on surfaces of both walls and dust particles, which for electrons can be considered in the Boltzmann equation for EEDF as volume recombination. Another of the main parameters affecting the distribution of dusty plasma is the total number of dust grains N_{tot}. In experiments, this parameter is difficult to control. The number of dust particles and the radial profile of their distribution in space are formed self-consistently. In the calculations, it is possible to establish various values of the total number of dust particles per unit length (per 1 cm) of the positive column, which is equal to the integral of the particle density over the cross section of the discharge tube.

Using calculations by this model, it was found that for values of the discharge current $I_d < 8$ mA, clouds of dust particles have the usual compact structures. In this case, voids in the cloud do not appear, and the N_d distribution has a uniform decaying radial profile with a maximum in the center of the discharge tube. With the increase of current I_d, the density of dust particles N_d in the center of the cloud decreases. At $I_d > 10$ mA, the particles in the cloud move away from the center of the discharge tube to the periphery. With a further increase in I_d, the radius of voids increases, and the cloud of dust particles has a “cup-shaped” structure without particles in the upper and central parts of the cloud. In Figure 1, dust particle density radial distributions for discharge currents 8 mA and 13.4 mA are presented.

An analysis of papers (see, for example, [22]) devoted to studies of the formation of voids in dusty plasmas shows that a void is formed in RF discharges when the electrostatic force becomes less than the ion drag force (assuming that other forces are negligible). If the ion drift $u_i = \mu_i E$ is proportional to the electric field strength E, the ratio of F_{id} and F_E can be represented as [22]: $|F_{id}/F_E| \sim \mu_i n_i Z_d$, i.e. the ratio is proportional to the charge of dust particles Z_d, ion density n_i and ion mobility μ_i,. An estimate in [22] showed that the condition $|F_{id}/F_E| > 1$ can be achieved at low gas pressures $\mu_i \sim 1/p$, high discharge currents $n_i \sim I_d$, and for large dust particles $Z_d \sim r_d$. In the case of a direct current discharge with cylindrical symmetry, voids are formed on the axis of the discharge tube. The radial component $F_{id}(r)$, as well as the radial component $F_{th}(r)$, expels dust grains from the center of the dust cloud to the periphery, despite the electrostatic force $F_E(r)$, which traps particles on the axis of the discharge tube. In voids, the condition $|F_{id}/F_E| > 1$is satisfied. At Figure 2 radial distributions of the product of dust particle density and the forces acting on dust particles for discharge currents 8 mA and 13.4 mA are presented.

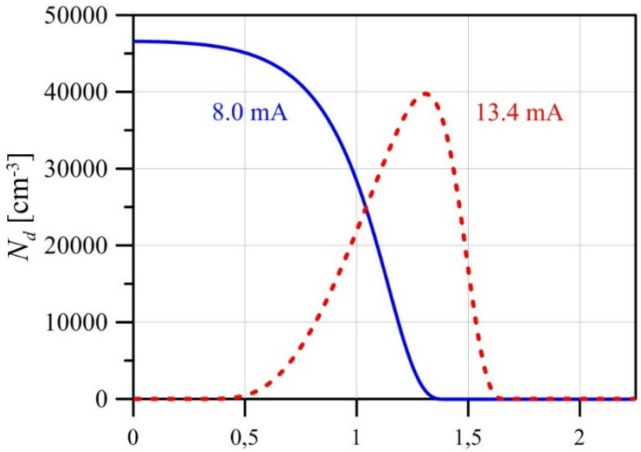

Figure 1 - Dust particle density radial distributions for discharge currents of 8 mA and 13,4 mA, gas pressure 0,38 Torr, dust particle diameter 2 μm. Solid line for I_d = 8 mA, dashed line for I_d = 13,4 mA.

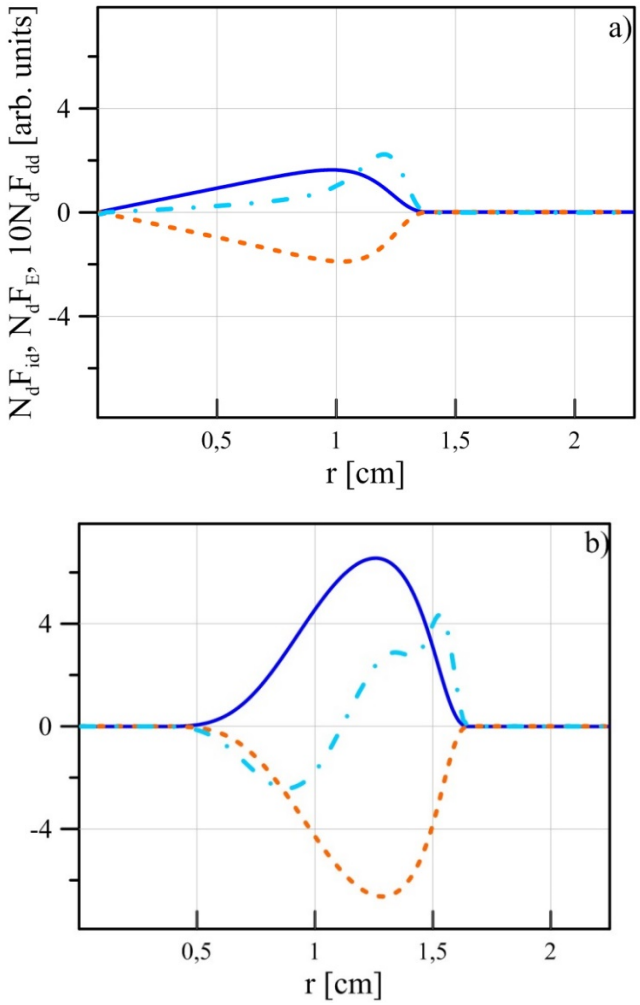

Figure 2 - Radial distributions of the product of dust particle density and the forces acting on dust particles: solid line for the ion drag force $F_{id}N_d$, dashed line for the electrostatic force F_EN_d , dashed dotted line for the interparticle repulsive force $F_{dd}N_d$. (a) I_d = 8 mA, (b) I_d = 13.4 mA.

4 Conclusions

It should be noted that the obtained conditions for the formation of voids are nontrivial. A simple increase in the discharge current (as well as a decrease in gas pressure or an increase in the particle radii or) by a factor of two will not lead directly to twice pronounced void. These parameters are highly dependent on each other self-consistently. If you increase the discharge current, then the electric field, axial and radial strengths, particle charge and other parameters will vary depending on each other.

Acknowledgments.

This work was carried out under state contract with IT SB RAS.

References

1. Fortov V. E. et al. Dusty plasmas // Phys. Usp. – 2004. – Vol. 47. – P. 447

2. Shukla P. K. Intense solitary laser pulse propagation in a plasma // Physics of Plasmas. – 2001. – Vol. 8. – P. 1791.

3. Ishihara O. Complex plasma: dusts in plasma: Plasma-aided fabrication of nanostructures and nanoassemblies // J. Phys. D. – 2007 – 40, R121-R147.

4. Thomas H., Morfill G.E., Demmel V. et al. Plasma crystal: Coulomb crystallization in a dusty plasma // Phys. Rev. Lett. – 1994. – Vol. 73. – No. 5. – P. 652-655.

5. Ramazanov T.S., Dzhumagulova K.N., Jumabekov A.N., Dosbolayev M.K. Structural properties of dusty plasma in direct current and radio frequency gas discharges // Phys. Plasmas. – 2008. – Vol. 15. – No. 5. – P. 053704.

6. Fortov V.E., Nefedov A.P., Torchinskii V.M. et al. Crystallization of a dusty plasma in the positive column of a glow discharge // J. Exp. Theor. Phys. Lett. – 1996. – Vol. 64. – No. 2. – P. 92-98.

7. Sukhinin G.I., Fedoseev A.V., Ramazanov T.S. et al. Non-local effects in a stratified glow discharge with dust particles // J. Phys. D. – 2008 – 41, 24, 245207.

8. Thomas E. Dust clouds in Dc-generated dusty plasmas: Transport, waves, and three-dimensional effects // Contrib. Plasma Phys. – 2009. – Vol. 49. – No. 4-5. – P. 316-345.

9. Fortov V., Morfill G., Petrov O. et al. The project 'Plasmakristall-4' (PK-4)–a new stage in investigations of dusty plasmas under microgravity conditions: first results and future plans // Plasma Phys. Control. Fusion. – 2005. – Vol.47. –No. 12b. – P. B537.

10. Mitic S., Klumov B.A., Khrapak S.A., Morfill G.E. Three dimensional complex plasma structures in a combined radio frequency and direct current discharge // Phys. Plasmas. – 2013. – Vol.20. – No. 4. – P. 043701.

11. Morfill G.E., Thomas H.M., Konopka U. et al. Condensed plasmas under microgravity // Phys. Rev. Lett. – 1999. – Vol. 83. – No. 8. – P. 1598-1601.

12. Bockwoldt T., Arp O., Menzel K.O., Piel A. On the origin of dust vortices in complex plasmas under microgravity conditions // Phys. Plasmas. – 2014. – Vol.21. –No. 10. – P. 103703.

13. Goree J., Morfill G.E., Tsytovich V.N., Vladimirov S.V. Theory of dust voids in plasmas // Phys. Rev. E. – 1999. – Vol. 59. – No. 6. – P. 7055-7067.

14. Tsytovich V.N., Vladimirov S.V., Morfill G.E., Goree J. Theory of collision-dominated dust voids in plasmas // Phys. Rev. E. – 2001. – Vol.63. –No.5. – P. 056609.

15. Akdim M.R., Goedheer W.J. Modeling of voids in colloidal plasmas // Phys. Rev. E. – 2001. – Vol. 65. –No. 1. –P. 015401.

16. Boeuf J.P. Characteristics of a dusty nonthermal plasma from a particle-in-cell Monte Carlo simulation // Phys. Rev. A – 1992. – Vol.46. –P. 7910.

17. Sukhinin G. I., Fedoseev A. V., Antipov S. N., Petrov O. F., Fortov V. E. Influence of dust particles concentration on plasma parameters in DC discharge // Contributions to Plasma Physics. – 2009. – Vol. 49. – No.10. – P. 781–785.

18. Sukhinin G. I., Fedoseev A. V. Influence of dust-particle concentration on gas-discharge plasma // Physical Review E. – 2010. – Vol.81. – No.1. – P. 016402.

19. Fedoseev A.V., Sukhinin G.I., Ramazanov T.S., Kodanova S.K., Bastykova N.H. Interaction between glow discharge plasma and dust particles // Thermophysics and Aeromechanics. – 2011. – Vol.18. – No. 4. – P.615–627.

20. Sukhinin G.I., Fedoseev A.V. Radial distributions of dusty plasma parameters in a DC glow discharge // Contributions to Plasma Physics. – 2012. – Vol. 52. – No.9. – P. 756–760.

21. Sukhinin G.I., Fedoseev A.V., Antipov S.N., Petrov O.F., Fortov V.E. Dust particle radial confinement in a dc glow discharge // Physical Review E. – 2013. – Vol. 87. – No.1. – P. 013101.

22. Fedoseev A.V., Sukhinin G.I., Dosbolayev M.K., Ramazanov T.S. Dust-void formation in a dc glow discharge // Physical Review E. – 2015. – Vol. 92. – No. 2. – P. 023106.

23. Fedoseev A. V., Sukhinin G. I., Abdirakhmanov A. R., Dosbolayev M. K., Ramazanov T. S. Voids in dusty plasma of a stratified DC glow discharge in noble gases // Contributions to Plasma Physics. – 2016. – Vol.56. – No. 3-4. – P. 234–239.

24. Totsuji H. Simple model for fine particle (dust) clouds in plasmas // Physics Letters A. – 2016. – Vol. 380. – No.16. – P. 1442–1445.

25. Shumova V.V., Polyakov D.N., Vasilyak L.M. Neon dc glow discharge at cryogenic cooling: experiment and simulation // Journal of Physics D: Applied Physics. – 2017. – Vol. 50. – No. 40. – P. 405202.

26. Polyakov D.N., Shumova V.V., Vasilyak L.M. Positive column of a glow discharge in neon with charged dust grains (a review) // Plasma Physics Reports. – 2017. – Vol. 43. – No. 3. – P. 397–404.

27. Shumova V. V., Polyakov D. N., Vasilyak L. M. Influence of dust void on neon DC discharge // Plasma Sources Science and Technology. – 2017. – Vol. 26. – No.3. – P. 035011.

28. Tian R., Yuan Ch., Li H., Liang Y., Wu J., Kudryavtsev A. A., Kirsanov G. V., Zhou Zh., Jiang Yo. Influence of dust particles on positive column of DC glow discharge // Journal of Applied Physics. – 2018. – Vol.123, – No.10. – P. 103301.

29. Sukhinin G.I., Fedoseev A.V., Antipov S.N., Petrov O.F., Fortov V.E. Effect of trapped ions and nonequilibrium electron-energy distribution function on dust-particle charging in gas discharges // Physical Review E. – 2009. – Vol. 79. – No.3. – P. 036404.

30. Sukhinin G., Fedoseev A., Antipov S., Petrov O., Fortov V. Trapped ions and the shielding of dust particles in low-density non-equilibrium plasma of glow discharge // Journal of Physics A: Mathematical and Theoretical. – 2009. – Vol. 42. – No.21. – P. 214027.

IRSTI 41.27.29, 89.51.17 https://doi.org/10.26577/phst.2020.v7.i2.02

Physical properties of dark matter in galaxy U11454

K. Boshkayev[1], T.K. Konysbayev[2], E.B. Kurmanov[2],
M. Muccino[3,*] and G. Zhumakhanova[1]

[1]*International Center for Relativistic Astrophysics, 10, Republic square, I–65122 Pescara, Italy*
[2]*School of Science and Technology, University of Camerino,*
16, Via Andrea D'Accorso, 62032, Camerino, Italy
[3]*National Institute of Nuclear Physics (INFN), National Laboratory of Frascati,*
54, Via Enrico Fermi, 00044 Frascati, Italy
[*]*e-mail: marco.muccino@lnf.infn.it*

In this paper physical characteristics of dark matter distribution in the spiral galaxy U11454 is explored using only well-known cored density profiles in the literature such as the pseudo-isothermal, Burkert, Einasto, exponential sphere, Beta and Brownstein profiles. It is presumed that the distribution of dark matter in the considered galaxy is spherically symmetric without taking into account its complex structural components. It is assumed that dark matter possesses non-vanishing pressure which allows theoretically analyzing the state parameter. The model free parameters of each profile are inferred from the rotation curve data of the galaxy by means of non-linear model fit procedure. Using the Bayesian Information Criterion the best fit profile among the considered ones is selected. Furthermore, the hydrostatic equilibrium equation is solved and the pressure profiles for each above mentioned density profile are constructed in the weak gravitational field regime. Combining the pressure and corresponding density profiles one gains equations of state for the dark matter in the galaxy U11454. The mass and gravitational potential are evaluated and constructed as a function of the radial distance for each profile. The total dark matter mass is assessed and our results are confronted and contrasted with the previous outcomes. In addition, the speed of sound is estimated in the dark matter distribution and it is shown that its behavior is quite unusual especially for the Brownstein profile. Finally, the refracting index is calculated in order to assess gravitational lensing effects produced by the presence of dark matter and astrophysical implications of the obtained results are discussed.

Key words: dark matter, rotational curves, equation of state, speed of sound and refractive index.
PACS number: 95.35.+d, 98.35.−a

1 Introduction

Dark matter (DM) interacts with ordinary matter via gravity. For this reason it is inaccessible to direct observations and measurements. Recent cosmological surveys have demonstrated that DM represents the 26.8 % of the total energy budget of the Universe [1]. So far, from a theoretical viewpoint it was assumed that DM consists of some experimentally undiscovered particles derived from the extension of the standard model of particle physics [2, 3].

Astronomers and astrophysicists indirectly receive all information about DM from rotation curves (RCs) of galaxies and gravitational lensing effects. RCs represent profiles of linear velocity $v(r)$ of stars and gas in circular orbits as functions of radial distance r from the galactic center to the outer parts. The RCs of galaxies have an amplitude that remains almost constant with increasing distance, even outside the stellar disk, which is not normally expected in Newtonian gravity (NG) [4, 5]. According to some studies it is presumed that the DM consists of nonrelativistic and collisionless particles, whose cross sections lie around $\sim 10^{-26}$ cm^2 [6].

In this work to study the distribution of DM in the chosen galaxy we mainly consider widely used density profiles such as: the pseudo-isothermal (ISO), Burkert, Beta, Brownstein, Einasto and exponential sphere in the framework of NG. By analyzing the RCs data points we derive the unknown model parameters of the DM halo for all profiles. In analogy to our previous work [7] we suppose that the DM equation of state (EoS) in a particular galaxy, by default, do not depend upon

the density profiles. Hence, we intend to check whether this assumption is valid or not for the galaxy U11454 as well. Moreover, to avoid the cuspy halo problem we mainly focus on the cored density profiles. This treatment is consistent with the fact that the DM density and pressure at the galactic center must be finite.

Following Ref. [7] we solve the hydrostatic equilibrium equation within NG to find the pressure profiles. The DM EoS for galaxy U11454 can be obtained by expressing pressure in terms of density for each individual model. For some profiles EoS is obtained analytically, but for others this can be done numerically only. Thus, the main objective of this work is to test whether the DM EoS depends on the adopted density profile or not. Using the DM EoS, we calculate the speed of sound and also the refractive index, which play a pivotal role in the formation of structures and in the gravitational lensing effect.

The paper is organized as follows. The DM phenomenological profiles and their characteristics are presented in section 2. The basic equation and their analytic solutions are displayed in section 3. The fitting methods of the observational data of U11454 RC and the major numerical results on the EoS, speed of sound and refractive index are rendered in section 4. Conclusions and perspectives of our work are summarized in section 5.

2 Phenomenological dark matter profiles

The distribution of DM in galaxies is not uniform, concentrating at their centers and dropping off at the periphery. Using the methods of numerical simulation of the dynamics of stars in galaxies, one can find the corresponding DM distribution function or its profile. In this paper, we have chosen traditionally used cored DM density profiles, such as the pseudo-isothermal, Beta, Burkert, Brownstein, Einasto and exponential sphere. All profiles that we used in this work are characterized by two parameters: the DM density at the centers of galaxies or the characteristic density ρ_0 and the scale radius r_0, except for the Einasto profile, which has one more free parameter.

Thus, we employ the following models:

1. The ISO profile [8]:

$$\rho_{Iso}(r) = \frac{\rho_0}{1+x^2}, \tag{1}$$

where $x = x(r) = r/r_0$, r is the radial coordinate/distance. The model depends upon the two constants r_0 and ρ_0, so do the following profiles.

2. Exponential sphere [9]:

$$\rho_{Exp}(r) = \rho_0 e^{-x}. \tag{2}$$

3. Burkert profile [10]:

$$\rho_{Bur}(r) = \frac{\rho_0}{(1+x)\left(1+x^2\right)}. \tag{3}$$

4. The Beta profile with $\beta = 1$ [11, 12]:

$$\rho_{Beta}(r) = \frac{\rho_0}{\left(1+x^2\right)^{3/2}}. \tag{4}$$

5. Brownstein profile [12, 13]:

$$\rho_{Bro}(r) = \frac{\rho_0}{1+x^3}. \tag{5}$$

6. Einasto profile [14]:

$$\rho_{Ein}(r) = \rho_0 \exp\left[2\alpha\left(1-x^{1/\alpha}\right)\right], \tag{6}$$

where α is the Einasto free parameter, which determines the slope of the profile [15].

In Figure 1 we illustrate the dependence of ρ/ρ_0 on r/r_0 for various phenomenological DM halo profiles. In this dimensionless representation the profiles depict diverse behavior especially at large distances. Note that ρ_0 and r_0 are different for each profile. The central density for the Einasto profile is determined as $\lim_{r\to 0}\rho_{Ein}(r) = \rho_0 e^{2\alpha}$.

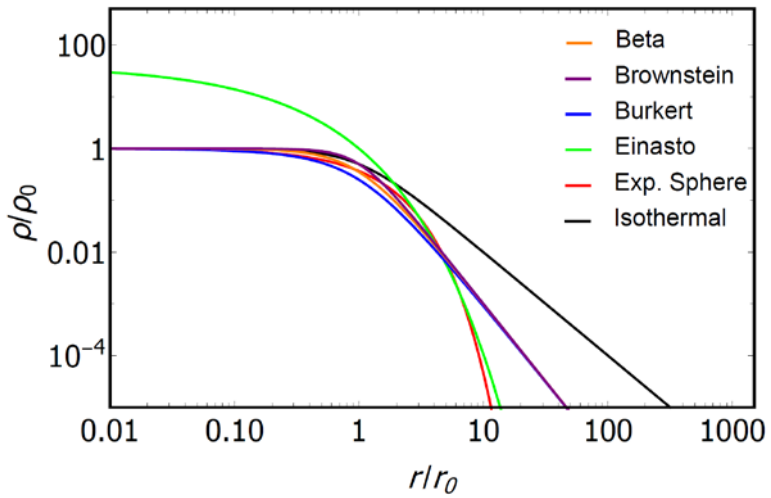

Figure 1 – Color online. Different phenomenological DM density profiles. For the Einasto profile we use $\alpha = 1.8$ inferred from the RC data points

3 Equations of hydrostatic equilibrium and analytic results

The main goal of this work is to obtain the equation of state of DM in the NG regime. To do so we start with the standard Newtonian hydrostatic equilibrium equations, given by [16, 17]

$$\frac{dM(r)}{dr} = 4\pi r^2 \rho(r), \tag{7}$$

$$\frac{dP(r)}{dr} = -\rho(r)\frac{GM(r)}{r^2}, \tag{8}$$

$$\frac{d\Phi(r)}{dr} = \frac{GM(r)}{r^2}, \tag{9}$$

where $M(r)$ is the mass profile enclosed inside the sphere of radius r, $P(r)$ is the DM pressure, G is the Newtonian gravitational constant and $\Phi(r)$ is the gravitational potential. To obtain expressions for the pressure the density profiles Eqs. (1) – (6) are separately plugged in Eqs. (7) – (8). We integrate the expression for the pressure, using boundary conditions, imposing that P vanishes as r approaches infinity and P becomes finite as r tends to zero.

For the ISO, Beta and exponential sphere profiles all calculations were performed analytically, whereas for the Einasto, Brownstein and Burkert profiles all analyzes were carried out numerically. The pressure and EoS formulas for the ISO and exponential sphere profiles in Eqs. (1) and (2) are given in Ref. [7], for the Beta profile we obtain the following equation

$$M_{Beta}(r) = 4\pi r_0^3 \rho_0 \left\{ \operatorname{arsinh}(x) - \frac{x}{\sqrt{1+x^2}} \right\}, \tag{10}$$

$$P_{Beta}(r) = 4\pi G r_0^2 \rho_0^2 \left\{ \frac{1}{2\left(1+x^2\right)} + \frac{1+2x^2}{x\sqrt{1+x^2}} \operatorname{arsinh}(x) - 2\ln\left(2\sqrt{1+x^2}\right) \right\}, \tag{11}$$

$$\Phi_{Beta}(r) = -\frac{4\pi G r_0^2 \rho_0}{x} \left\{ \operatorname{arsinh}(x) - \frac{x}{\sqrt{1+X^2}} \right\}, \tag{12}$$

where $x = r/r_0$ as before, $X = R/r_0$ and R is the radius of the DM halo, evaluated by matching interior and exterior potentials. Since R is not well-defined quantity, usually, for practical purposes one sets it equal to the virial radius of the DM halo.

3.1 Dark matter equation of state

The EoS of a given fluid characterizes the physical features of the fluid itself and shows how it develops when it is not in equilibrium. Combining Eq. (11) together with Eq. (4), we obtain the EoS for the Beta profile

$$P_{Beta}(\rho) = 4\pi G r_0^2 \rho_0^2 \left\{ \frac{\xi}{2} + \frac{2-\xi}{\sqrt{\xi-1}} \operatorname{arsinh}\left(\sqrt{\frac{\xi-1}{\xi}} \right) - 2\ln\left(\frac{2}{\sqrt{\xi}} \right) \right\}, \quad (13)$$

where $\xi = \xi(\rho) = (\rho/\rho_0)^{2/3}$. Eq. (13) for the Beta profile has been obtained here for the first time.

Furthermore, the thermodynamic properties of the fluid are hidden inside the state parameter defined by [18]

$$\omega = \frac{P}{c^2 \rho}, \quad (14)$$

which is also known as a baratropic parameter. In our case, the pressure does not vanish inside the DM distribution and the corresponding formulas for the EoS are complicated for some profiles.

3.2 Speed of sound and refractive index

Using the speed of sound c_s, we can account for perturbations caused by the DM fluid. Its definition in case of adiabatic perturbations is [19]

$$c_s^2 = \left(\frac{\partial P}{\partial \rho} \right)_S. \quad (15)$$

The speed of sound for the ISO and exponential sphere profiles are given in Ref. [7] and for the Beta profile we find it from Eq. (13)

$$c_{s(Beta)}^2 = \frac{4\pi G r_0^2 \rho_0}{3} \frac{\sqrt{\xi}}{1-\xi} \times \times \left\{ \frac{1}{\sqrt{1-\xi}} \operatorname{arsinh}\left(\sqrt{\frac{1-\xi}{\xi}} \right) - 1 \right\}. \quad (16)$$

Additionally, we calculate and show that DM gives a refractive index which is slightly larger than pure vacuum. This can be seen when studying the optical properties of the galaxy under consideration. Thus, we here examine the refractive index of DM halo of the galaxy U11454 for all adopted profiles. The refractive index in the field of DM in the weak field regime is given by [20]

$$n(r) = 1 - \frac{\Phi(r)}{c^2} - \int \frac{GM(r)}{c^2 r^2} dr, \quad (17)$$

where $\Phi(r)$ is the internal gravitational potential for a given DM density profile, obtained by solving Eq. (9) and c is the speed of light in vacuum. The integration is carried out within the range of the radial coordinate taken from the RC data points.

4 Methods, analyses and numerical results

We aim to show that as a result of our analysis, by testing different profiles for such a galaxy, DM halo density law can be accounted for the kinematics of the whole family of disk (spiral) galaxies like U11454. For completeness, it is important to stress that the contributions of gas in the bulge and disk of the galaxy are crucial to characterize the RCs. In turn, the RC allows one to determine the distribution of the galaxy's mass along the radial distance. In the standard approach, all the constituents of the galaxy must be accounted for in analogy with Ref. [9]. However their contributions with respect to the DM halo are small. Moreover the inner parts of U11454 is not fully reported in the literature. Therefore, one can neglect the contribution of all the constituents of the galaxy, apart from the halo, for simplicity and adopt

$$\upsilon_{tot}^2 \simeq \upsilon_{profile}^2, \quad (18)$$

where $\upsilon_{profile}$ is the contributions of the DM halo profile velocity. So, $\upsilon_{profile}$ is defined by

$$\upsilon_{profile} = \upsilon(r) = \sqrt{\frac{GM(r)}{r}} \text{ and}$$

$$M(r) = \int_0^r 4\pi r^2 \rho(r) dr, \qquad (19)$$

where the DM mass $M(r)$ has been obtained by integrating Eq. (7), exploiting Eqs. (1) – (6).

Further, we apply the Levenberg-Marquardt nonlinear least squares method [21, 22] to find the minimum of the χ^2 function. The Levenberg-Marquardt algorithm is an iterative technique that locates the minimum of a function which is expressed as the sum of squares of nonlinear functions. It consists in a combination of the Gauss–Newton algorithm and the method of the steepest descent gradient. So, the χ^2 function is defined by

$$\chi^2 = \sum_{i=1}^{N} \left[\frac{\upsilon_i^{obs} - \upsilon(\rho_0, r_0, r)}{\sigma_{\upsilon,i}^{obs}} \right]^2, \qquad (20)$$

where υ_i^{obs} and $\sigma_{\upsilon,i}^{obs}$ are the N data points of U11454 RC and their corresponding errors, respectively (see Fig. 2, Top panel), while $\upsilon(\rho_0, r_0, r)$ is given by Eq. (19) and describes the RCs for each DM profile. The best fit parameters, minimizing the χ^2 for each DM profile are listed in Table 1 and shown in Figure 2 (Top panel). The ρ_0 and r_0 parameters listed in Table 1 are in agreement with the results of Ref. [23]. The amount of DM mass in the galaxy, computed by using different profiles, is also shown in Table 1 and it is shown to be consistent with the results of Ref. [23] for the ISO and Burkert profiles. The χ^2 values are also shown in the last column of Table 1.

Table 1 – Model parameters for galaxy U11454. We report for each profile ρ_0, r_0 and the masses expressed in units of solar mass $M_\odot$ with their error bars, respectively. The last two columns present the BIC statistical outputs and corresponding chi squares used for computing the BIC values. r_{vir} denotes the virial radius determined as the radius at which the density is equal to the critical density of the Universe multiplied by 200 and M_{vir} is the corresponding virial mass. [a] DM mass is calculated using the last data point in the halo for r. [b]DM mass is calculated using the scale radius r_0. [c]The values $\mathrm{BIC} \equiv \{84, 91, 79, 76, 85, 67\}$ are for the Beta, Brownstein, Burkert, Einasto, exponential sphere and ISO, respectively; we define $\Delta\mathrm{BIC} \equiv \mathrm{BIC} - \mathrm{BIC}_0$, with $\mathrm{BIC}_0 = 67$ the Isothermal reference value. For the Einasto profile $\alpha = 1.8 \pm 0.3$.

Profiles	$\rho_0 \pm \sigma_{\rho_0}$, ($10^{-3}\ M_\odot/pc^3$)	$r_0 \pm \sigma_{r_0}$ (kpc)	r_{vir}, (kpc)	M_{vir}, ($10^{10}\ M_\odot$)	$M \pm \sigma_M$ [a], ($10^{10}\ M_\odot$)	$M \pm \sigma_M$ [b], ($10^{10}\ M_\odot$)	ΔBIC[c]	χ^2
Beta	104.0 ± 10.8	3.7 ± 0.2	56.8	15.6	6.0 ± 1.0	1.1 ± 0.3	17	1.5
Brownstein	81.0 ± 10.0	3.6 ± 0.3	51.7	12.7	5.7 ± 1.2	1.1 ± 0.4	24	2.8
Burkert	139.0 ± 12.9	3.7 ± 0.2	62.3	18.6	6.1 ± 0.9	1.1 ± 0.3	12	1.0
Einasto	10.5 ± 2.6	7.2 ± 0.9	42.5	14.0	6.4 ± 2.2	3.4 ± 2.0	9	0
Exp. Sphere	130.9 ± 12.9	2.8 ± 0.2	24.1	7.5	5.9 ± 1.0	0.6. ± 0.2	18	1.7
ISO	151.0 ± 11.7	1.9 ± 0.1	142.8	98.6	6.5 ± 0.8	0.3 ± 0.1	0	0.4

To compare the selected 6 profiles, which have different number of parameters and are not nested into each other, we employ the Bayesian Information Criterion (BIC) [24]. BIC is a selection criterion among a finite set of models, conceived to solve the overfitting issue when increasing the number of parameters in the fitting function. For completeness, notice that other selection criteria could also be used, e.g. the Akaike information and/or DIC criteria [25, 26]. Starting from the χ^2 definition, the BIC is defined as

$$\mathrm{BIC} = \chi^2 + k \ln \mathrm{N}, \qquad (21)$$

where k is the number of model parameters. For the Einasto profile $k = 3$, while for all the other profiles $k = 2$. A profile with a minimum BIC value is favored, according to Ref. [27]. As one can see from Table 1 for galaxy U11454 the BIC value is minimum for the ISO profile and is maximum for the Brownstein profile, though the difference between the values is not large.

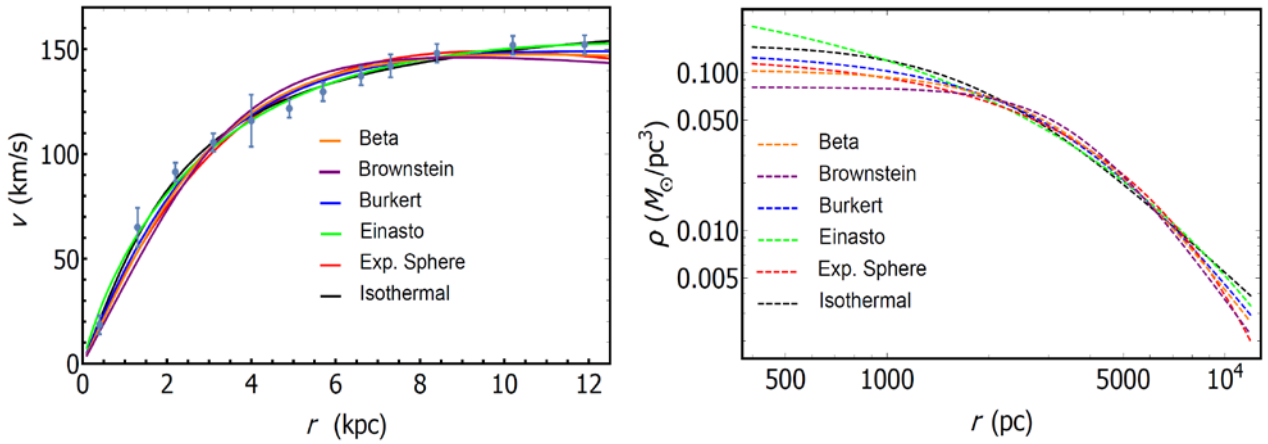

Figure 2 – Color online. Top panel: RC of galaxy U11454 and fitted profiles.
Bottom panel: Logarithmic density profiles of DM in the halo.

In Figure 2 (Top panel) we construct RC of galaxy U11454 and theoretical curves for different profiles adopted in this work. Here the gray thick points show the observational data with their error bars, solid curves show fitted ISO (black), exponential sphere (red), Einasto (green), Burkert (blue), Beta (orange) and Brownstein (purple) profiles. In the Bottom panel we present the density profiles with inferred model parameters from the fit.

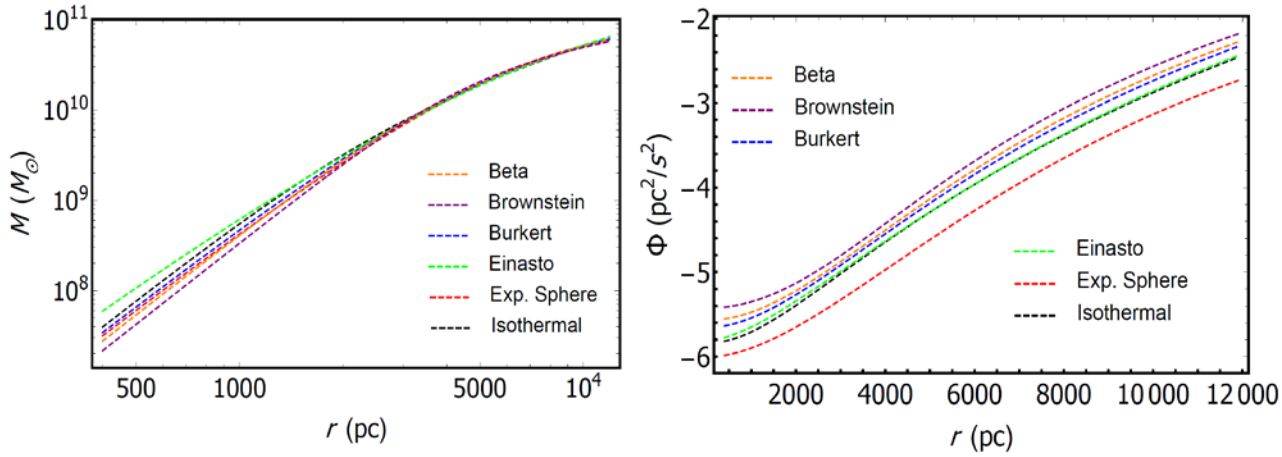

Figure 3 – Color online. Top panel: Logarithmic mass profiles of DM in the halo.
Bottom panel: Logarithmic gravitational potential of DM in the halo.
Note that $\Phi(r)$ is multiplied by 10^{-23}

In Figure 3 the mass in units of solar mass is plotted as a function of the radial coordinate (Top panel). At large distances all profiles produce similar mass. Correspondingly, the internal gravitational potential is illustrated as a function of the radial coordinate in the considered range (Bottom panel). The behavior of the potential for various profiles is almost identical.

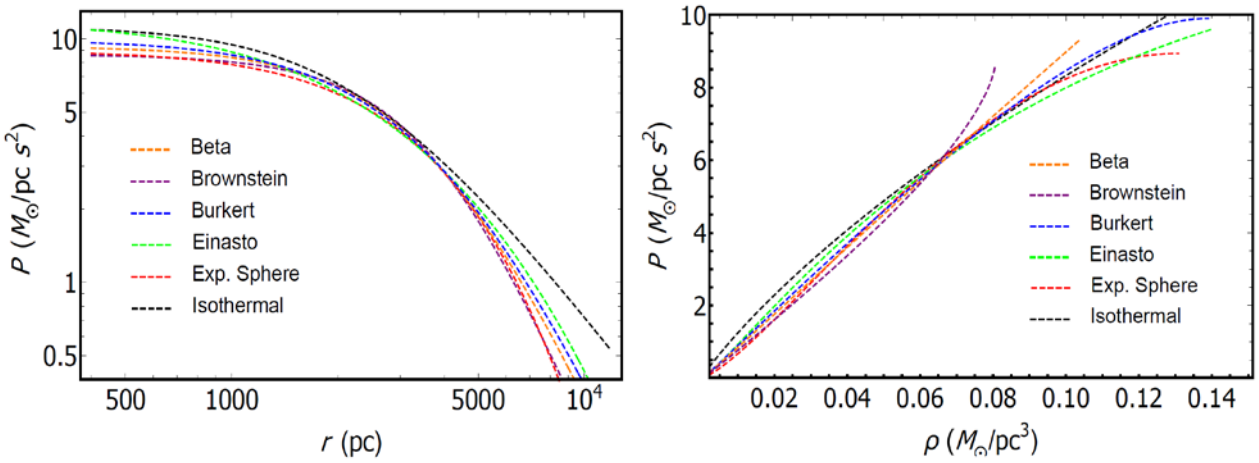

Figure 4 – Color online. Top panel: Logarithmic pressure profiles of DM in the halo. Bottom panel: The equation of state of DM halo. Note that P in both panels is multiplied by 10^{-25}

In Figure 4 we plotted the pressure profiles $P(r)$ (Top panel) and equation of state $P(\rho)$ (Bottom panel) for galaxy U11454, using all the DM halo models i.e. Eqs. (1) – (6), by solving Eqs. (7) – (8). Here one can choose different units by using the following conversion factors for the density and pressure:

$$1\mathrm{M}_\odot/\mathrm{pc}^3 = \\ = 6.77\times10^{-23}\,\mathrm{g}/\mathrm{cm}^3 = \\ = 38.05\left(\mathrm{GeV}/c^2\right)/\mathrm{cm}^3$$

and

$$1\mathrm{M}_\odot/(\mathrm{pc\,s}^2) = \\ = 6.44\times10^{14}\,\mathrm{g}/\left(\mathrm{cm\,s}^2\right) = \\ = 3.62\times10^{38}\left(\mathrm{GeV}/c^2\right)/\left(\mathrm{cm\,s}^2\right),$$

respectively.

It is fascinating to study the general behavior of the EoS involving the state parameter ω. Consequently, (14) can be written either in terms of the radial coordinate r or density ρ, as shown in Figure 5. It follows that ω tends to zero for large distances or low densities, except for the ISO profile, where it becomes constant. At small distances or high densities, ω decreases or tends to a constant value, except for the Brownstein profile which grows in an unusual manner, at least in the considered range of distances provided by the RC data points.

In our calculations, we can also take into account the corrections provided by general theory of relativity. At large distances when $\rho << \rho 0$ the corrections can be neglected. However, near the central part of the galaxy, its deviations from NG would be significantly noticeable, since the corrections of general relativity in pressure are clearly much larger than in NG [28]. This is simply a consequence of the Tolman-Oppenheimer-Volkov system of equations.

Besides, in Figure 6 (Top panel) we plotted the speed of sound according to Eq. (15) for all the profiles. An unusual feature of DM is the fact that with increasing density, the speed of sound decreases for all profiles apart from the Brownstein profile where the opposite is true. It is known from cosmology that if the speed of sound in the central part of the DM distribution is less than in its outer parts, then it allows the formation of large-scale structures [29]. Thus, we can say and state that the Brownstein profile is not appropriate to form galaxies. Hence, one can rule it out.

It should be recalled that for the ISO, exponential sphere, Burkert, Beta and Brownstein profiles ρ_0 is the central density. However for the Einasto profile ρ_0 is the characteristic density and its central density is equal to $\rho_0 e^{2\alpha}$ as indicated above. As can be seen from Fig. 6 (Top panel), the behaviors of the curves for the speed of sound are very different, some of them change drastically as a function of the density. Our results are similar to the ones of Ref. [30], but for another galaxy.

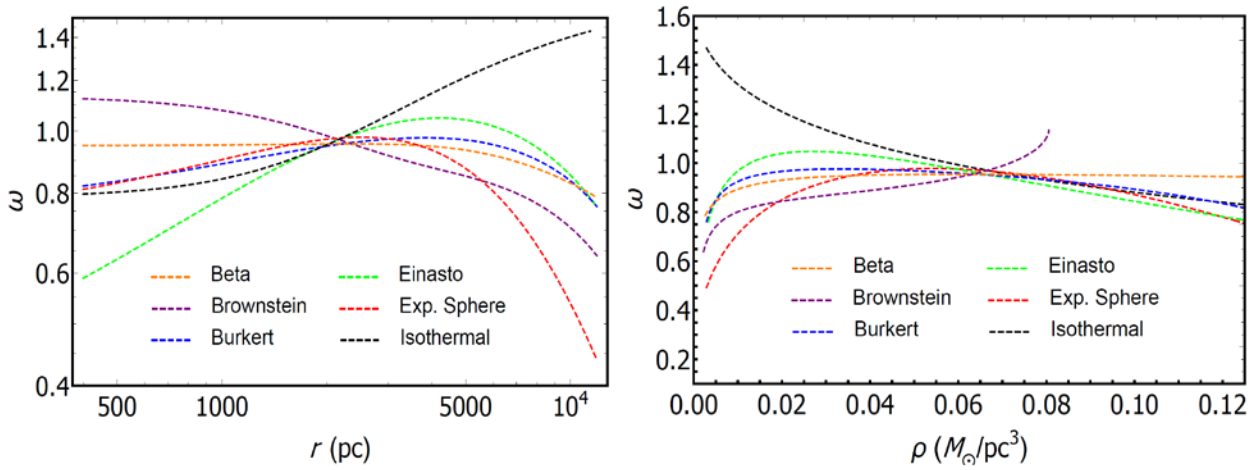

Figure 5 – Color online. Top panel: Dimensionless state parameter ω as a function of radial coordinate r. Bottom panel: Dimensionless state parameter ω as a function of density ρ. Note that ω in both panels is multiplied by 10^{-7}

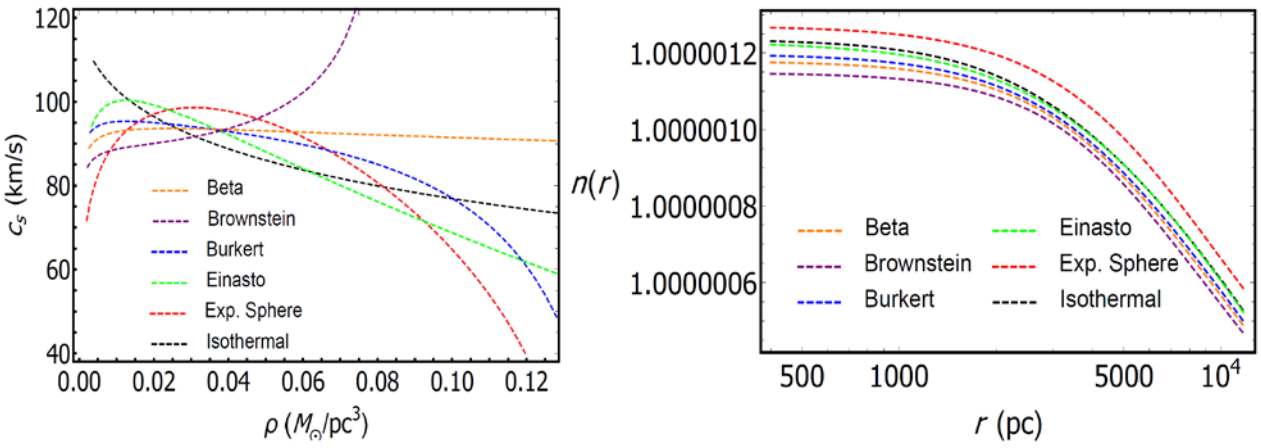

Figure 6 – Color online. Top panel: The speed of sound in the DM distribution for different profiles. Bottom panel: The refractive index for DM in galaxy U11454.

For the above considered profiles we have shown the dependence of the refractive index n on the radial coordinate in the DM distribution in Fig. (6) (Bottom panel). The value of the refractive index is small in the halo, as we expected. In the disk region the refractive index grows up slowly to the direction of the galactic center. In the core region the refractive index becomes almost constant. The overall change in the refractive index is extremely small, less than 1 part of 10^6. The refractive index in vacuum is slightly less than in DM for all the profiles that we used at a distance within

(0.4 – 11.9) kpc which corresponds to the RCs data points. In general, the refractive index can also be used to study the light propagation process in the epoch of DM dominance [31].

5 Conclusion

By analyzing the RC data points of the fuzzy spiral galaxy U11454, we inferred the free parameters of the models with the help of the least squares method. We used the well-known cored DM density profiles from the literature and, in addition, we considered the exponential sphere, Beta and Brownstein profiles for comparison. The exponential sphere profile is usually applied to study the inner parts of galaxies [9] and, in fact, for galaxy

U11454 it showed a good result. This can be seen from Table 1.

Out of all the considered profiles, the Brownstein profile has the highest BIC value, and the ISO profile has the lowest value. The same is true also for the χ^2. The difference in the BIC between ISO profile (with the smallest value) and Brownstein profile (with the highest value) is $\Delta\mathrm{BIC} = 24$ and exhibits very strong evidence against the Brownstein profile. Among other profiles, the only one with the least evidence against it, though still strong, is the Einasto profile with $\Delta\mathrm{BIC} = 9$. So, for our purposes the ISO and Einasto profiles are the most convenient profiles to study the DM EoS of the galaxy U11454.

Inspecting the curves for $\rho(r)$, $P(r)$ and $P(\rho)$, we have seen that the behavior of the profiles is similar to each other, but the degeneracy among the profiles is completely broken by looking at the diagram of the speed of sound. Here all profiles are distinct. As can be seen in Fig. 6 (Top panel), the speed of sound for the Brownstein profile behaves completely differently and does not allow to form structures.

Moreover we calculated the virial radius and corresponding mass. For that we used the condition when the density is equal to the critical density $\rho_{crit} = 9.31\times10^{-30}\,\mathrm{g/cm^3}$ [32] of the Universe multiplied by 200. The virial radius and corresponding mass turned out to be larger than the size of the galaxy inferred from the RC. Among the considered models the Isothermal profile produced the largest and the exponential sphere profile produced the smallest virial radius and corresponding mass.

In conclusion our analyzes demonstrate that for the considered galaxy the Isothermal, Einasto and Burkert profiles are the best models as they have the smaller BICs than the exponential sphere, Beta and Brownstein profiles. In accordance to our recent findings [7, 33, 34] the assumption that the EoS of DM do not depend on the model turned out to be partially valid only in a limited range of densities.

The features of DM such as the equation of state (the state parameter), refractive index and sound speed depend on the adopted models. If for the equation of state and refractive index the differences are extremely small, however for the sound speed the differences are quite noticeable. Therefore to explore the nature of DM one should attentively analyze DM profiles, accurately assess the value of BIC and rigorously examine the behavior of the sound speed. It would be also interesting to continue studies in this direction including contributions from the gas and disk, taking into account a composite structure of the galaxy. This issue will be addressed in our future works.

Acknowledgements. The work was supported by the Ministry of Education and Science of the Republic of Kazakhstan Grant: IRN AP08052311.

References

1. Planck Collaboration, Ade P.A.R. e.a.P.C. Planck 2013 results. I. Overview of products and scientific results // Astronomy and Astrophysics. – 2014. – Vol. 571. – A1.
2. Bertone G., Hooper D., Silk J. Particle dark matter: evidence, candidates and constraints // Physics Reports. – 2005. – V. 405. – P. 279-390.
3. Schumann M. Direct detection of WIMP dark matter: concepts and status // Journal of Physics G: Nuclear and Particle Physics. – 2019. – Vol. 46. – P. 103003.
4. Einasto J., Kaasik A., Saar E. Dynamic evidence on massive coronas of galaxies // Nature. – 1974. – Vol. 250. – P. 309–310.
5. Rubin V.C., Burstein D., Ford W. K. J., Thonnard N., Rotation velocities of 16 SA galaxies and a comparison of Sa, SB and SC rotation properties // Astrophysical Journal. – 1985. – Vol. 289. – P. 81–104.
6. Jungman G., Kamionkowski M., Griest K., Supersymmetric dark matter // Physics Reports. – 1996. – Vol. 267. – P. 195–373.
7. Boshkayev K., Konysbayev T., Kurmanov E., Luongo O., Muccino M. Imprint of Pressure on characteristic dark matter profiles: The case of ESO0140040 // Galaxies. – 2020. – Vol. 8. – P. 74.
8. Jimenez R., Verde L., Oh S.P. Dark halo properties from rotation curves // Monthly Notices of the Royal Astronomical Society. – 2003 – Vol. 339. – P. 243–259.
9. Sofue Y. Rotation curve and mass distribution in the galactic center – from black hole to entire galaxy // Publications of the Astronomical Society of Japan. – 2013 – Vol. 65. – P. 118.

10. Burkert A. The structure of dark matter halos in dwarf galaxies // The strophysical Journal Letters. – 1995 – Vol. 447. – L25–L28.

11. Navarro J.F., Frenk C.S., White S.D.M. Simulations of X-ray clusters // Monthly Notices of the Royal Astronomical Society. – 1995 – Vol. 275. – P. 720–740.

12. Sofue Y. Rotation curve of the Milky Way and the dark matter density // Galaxies. – 2020 – Vol. 8. – P. 37.

13. Brownstein J.R., Moffat J.W. Galaxy rotation curves without nonbaryonic dark matter // The Astrophysical Journal. – 2006 – Vol. 636. – P. 721–741.

14. Merritt D., Graham A.W., Moore B., Diemand J., Terzic B. Empirical models for dark matter halos. I. Nonparametric construction of density profiles and comparison with parametric models // The Astronomical Journal. – 2006 – Vol. 132. – P. 2685–2700.

15. Einasto J. On the construction of a composite model for the galaxy and on the determination of the system of galactic parameters // Trudy Astrofizicheskogo Instituta Alma-Ata. – 1965 – Vol. 5. – P. 87–100.

16. Shapiro S.L., Teukolsky S.A. Black holes, white dwarfs and neutron stars: The physics of compact objects. Wiley-VCH, 1986.

17. Misner C.W., Thorne K.S., Wheeler J.A. Gravitation. W. H. Freeman & Company: San Francisco, 1977.

18. Capozziello S., De Laurentis M., Luongo O., Ruggeri A. Cosmographic constraints and cosmic fluids // Galaxies. – 2013 – Vol. 1. – P. 216-260.

19. Capozziello S., D'Agostino R., Luongo O. Extended gravity cosmography // International Journal of Modern Physics D. – 2019 – Vol. 28. – P. 1930016.

20. Perlick V. Gravitational lensing from a spacetime perspective // Living Reviews in Relativity. – 2004 – Vol. 7. – P. 9.

21. Levenberg K. A method for the solution of certain non-linear problems in least squares // Quarterly of Applied Mathematics. – 1944 – Vol. 2. – P. 164–168.

22. Marquardt D. An algorithm for least-squares estimation of nonlinear parameters // Journal on applied mathematics. – 1963 – Vol. 11. – P. 431–441.

23. Garcia-Aspeitia M.A., Lopez-Dominguez J.C., Ortiz C. Hinojosa-Ruiz S., Rodriguez-Meza M.A. Energy density profile inspired by noncommutativity // Revista mexicana de física. – 2017– Vol. 63. – P. 423-438.

24. Schwarz G. D. Estimating the Dimension of a Model // Annals of Statistics. – 1963 – Vol. 6. – P. 461–464.

25. Akaike, H. A new look at the statistical model identification // IEEE Transactions on Automatic Control. – 1974 – Vol. 19. – P. 716–723.

26. Kunz M., Trotta R., Parkinson D.R., Measuring the effective complexity of cosmological models // Physical Review D. – 2006 – Vol. 74. – P. 023503.

27. Siutsou I., Argüelles C.R., Ruffini R. Dark matter massive fermions and Einasto profiles in galactic haloes // Astronomy Reports. – 2015 – Vol. 59. – P. 656–666.

28. Will C.M., The Confrontation between General Relativity and Experiment // Living Reviews in Relativity. – 2014 – Vol. 17. – P. 4.

29. Del Popolo A. Dark matter, density perturbations, and structure formation // Astronomy Reports. – 2007 – Vol. 51. – P. 169–196.

30. Barranco J., Bernal A., Núñez D. Dark matter equation of state from rotational curves of galaxies // Monthly Notices of the Royal Astronomical Society. – 2015 – Vol. 449. – P. 403–413.

31. Chechin, L.M., Kurmanov E.B., Konysbaev T.K. Geometrical Optics in a Universe with Dominance of Dark Matter // Russian Physics Journal. – 2020 – Vol. 63. – P. 58–63.

32. Di Paolo C., Salucci P., Erkurt A. The universal rotation curve of low surface bBottomness galaxies – IV.The interrelation between dark and luminous matter // Monthly Notices of the Royal Astronomical Society. – 2019. – Vol. 490. – P.5451 – 5477

33. Boshkayev K., Zhumakhanova G., Mutalipova K., Muccino M. Investigation of different dark matter profiles // News of the National Academy of Sciences of the Republic of Kazakhstan, Physico-Mathematical Series. – 2019. – Vol. 6. – No. 328. – P. 25 – 33.

34. Boshkayev K., Konysbayev T.K., Kurmanov E.B., Muccino M. Dark matter properties in galaxy U5750 // News of the National Academy of Sciences of the Republic of Kazakhstan, Physico-Mathematical Series. – 2020. – Vol. 6. – No. 334. – P. 81 – 90.

IRSTI 41.21.05; 41.21.19 https://doi.org/10.26577/phst.2020.v7.i2.03

February 25, 2014 solar flare data analysis in SunPy

A. Sarsembayeva[1,*], F. Belisarova[1],
M. Odsuren[2,†], A. Sarsembay[3]

[1]*Department of Physics and Technology, Al-Farabi Kazakh National University, 71, al-Farabi Ave., 050040, Almaty, Kazakhstan*
[2]*School of Engineering and Applied Sciences, National University of Mongolia, Ikh surguuliin gudamj 3, 14201, Ulaanbaatar, Mongolia*
[3]*School-Lyceum №250 named after T. Komekbayev, Balky bazar 19A, 120500, Karmakchi, Kyzylorda, Kazakhstan*
[*]*e-mail: sarsembaeva.a@kaznu.kz; †odsuren@seas.num.edu.mn*

Solar flares are strong radiation bursts, whereas large clouds of solar material and magnetic fields that erupt at high speeds from the Sun are coronal mass ejections. Harmful radiation from a flare does not pass through the atmosphere of the Earth to physically impact humans on the ground, but can disrupt the atmosphere in the layer where GPS and communication signals travel. Flares generate results across the entire electromagnetic spectrum. They emit x-rays and ultraviolet radiation, which means extremely high temperatures during a flash. Radio waves mean that tiny fractions of particles are accelerated to high levels of energy. Most of the radiation is synchrotron radiation produced along magnetic field lines by electrons traveling along spiral paths. In this paper was monitored solar flare registered on February 25, 2015. This flare, which peaked at 00:49 am EDT from a sunspot called Active Region 1990 (AR1990), is classified as an X4.9-class flare. We have performed solar data analysis using the Python/SunPy tool. SunPy was chosen as the principle data analysis environment since it provides easy to use interfaces to the Virtual Solar Observatory (VSO).

Key words: solar flares, emission measure, reconnection rate, SunPy.
PACS number(s): 96.60.−j; 96.60.Iv; 96.60.qe

Introduction

Solar-based flares are one of the most impressive energetic events in the solar atmosphere. Given their part of job in the solar corona's energy balance and their function playing important role in the space weather, numerous observations researched the release of energy and induction of solar flares, focusing on the solar active. National solar observatories are providing the overall network with a wealth of data, covering extensive time ranges (e.g. Solar and Heliospheric Observatory, SOHO), numerous perspectives (Solar Terrestrial Relations Observatory, STEREO), and returning a lot of information (Solar Dynamics Observatory, SDO) [1].

Solar and stellar flares have been studied using both ground and space-based investigation [2-3]. Currently, using GOES and soft X-ray data of *Yohkoh* Bragg crystal spectrometer, by [4] proposed between's the peak temperature of solar flares and their volume emission measure a exceptional correlation, where n is the electron number density and V is the volume. Shimizu [5] found a comparative connection in microflares observed by the *Yohkoh* soft X-ray telescope. Feldman, Laming, & Doschek [4] show that this relationship can also be effectively extrapolated to the instanse of stellar X-ray flares.

X-ray flare databases are used in our analysis. A dataset provided by the Geostationary Operational Environmental Satellite (GOES) [6] was used to collect the solar activity processes. According to their peak flux (W m−2) observed in the 0.1 to 0.8 nm wavelength range, GOES flares are classified as A, B, C, M, and X-class, corresponding to their peak flux. We selected the X-class flares corresponding to a flux in excess of 10−4 W m−2 at Earth, respectively. The GOES flare lists are available at NGDC/NOAA [7].

SunPy, an open-source and free community-developed solar data analysis package written in Python [8], was used in this research. Python/SunPy

was chosen as the key data analysis framework because it provides the Virtual Solar Observatory with easy to use interfaces (VSO). SunPy is a toolkit for data analysis that provides the requisite tools for Python's analysis of solar and heliospheric datasets. SunPy aims to provide the current standard, an IDL based solar data analysis environment known as SolarSoft (SSW) [9-13], with a free and open-source alternative.

In this work, we have observed solar flare occurred on Feb. 25, 2014. This flare, which peaked at 00:49 am EDT on Feb. 25, 2014from a sunspot called Active Region 1990 (AR1990), is classified as an X4.9-class flare.

2. Solar data visualization

To find and overplot the location of the brightest pixel, we first created the Map using the FITS data and imported the coordinate functionality. In the Figure 1 shown the brightest pixel location in different wavelengths obtained by Python/SunPy.

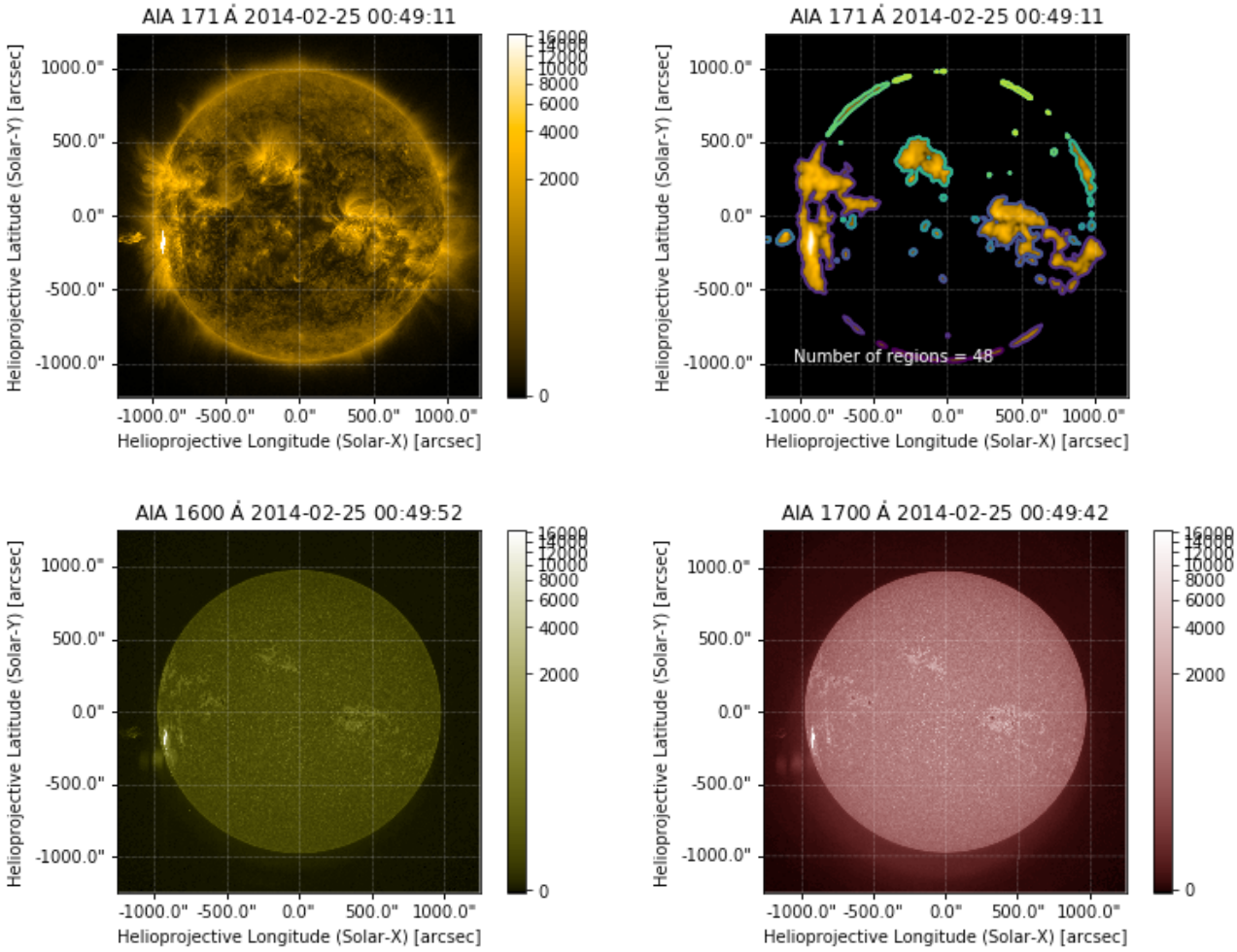

Figure 1 – The brightest pixel location (AR 1990 in AIA 171 Å, AIA 1600 Å and AIA 1700 Å)

To obtain the GOES flare intensity, we first grab GOES XRS data for a particular time of interest that is Feb. 25, 2014. Then the data loaded into a TimeSeries. Next we grab the HEK data for this time from the NOAA Space Weather Prediction Center (SWPC). The Figure 2 shows the Daily Synoptic Maps produced by the HMI on Feb. 25, 2014.

To enhance emission above the limb, we first created the Map using the FITS data. Next, we build two arrays, which include the entire x and y pixel indices. Then we converted this to helioprojective

coordinates and created a new array, which contains the normalized radial position for each pixel. Next, we plot it along with a fit to the data. We fit the logarithm of the intensity since the intensity drops of very quickly as a function of distance from the limb [14-15].

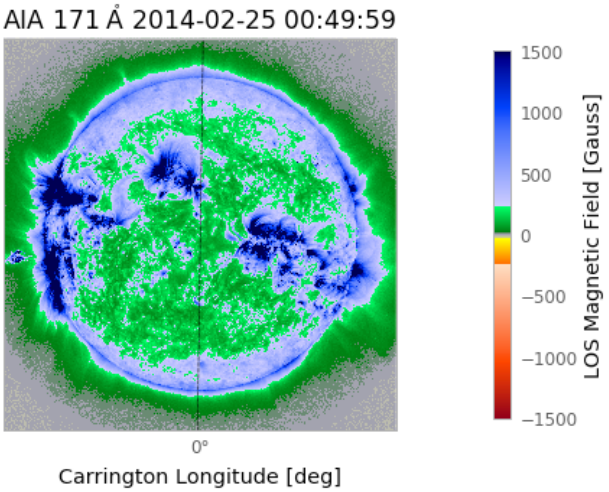

Figure 2 – Daily Synoptic Maps produced by the HMI

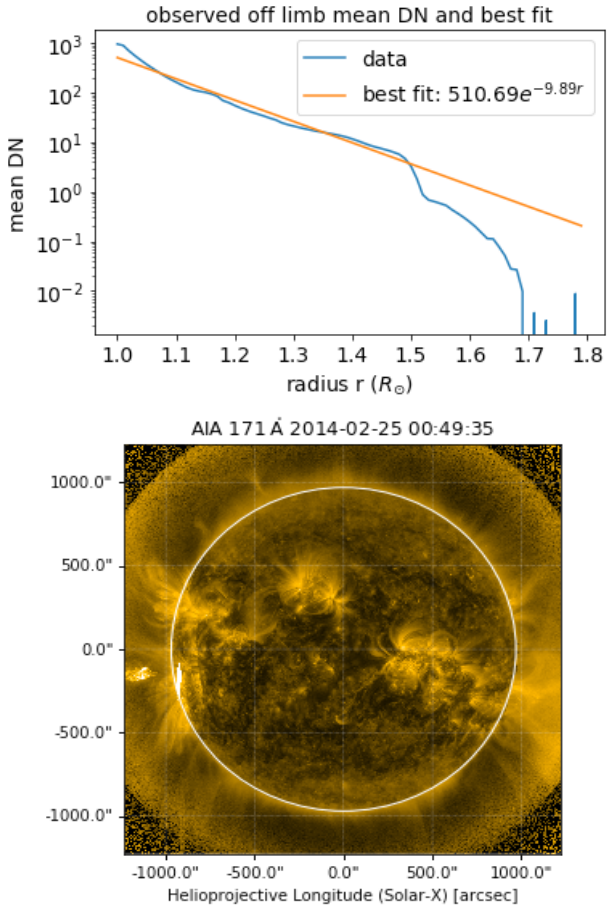

Figure 3 – Observed off limb mean DN and best fit

The National Oceanic and Atmospheric Administration (NOAA) is launching and maintaining a collection of satellites called Geostationary Operational Environmental Satellites with weather forecasting services (GOES). Each GOES satellite also includes a solar X-ray package (the «X-ray sensor» or XRS) consisting of a collimator that feeds a pair of ion chambers. Those ion chambers measure the Sun's spatially incorporated soft X-ray flux in two wavelength bands, 0.5-4 and 1-8Å, with a 3-s cadence. For 30 years, the GOES soft X-ray detectors have provided an essentially uninterrupted track of the activity of the Sun and are a valuable resource for the study of previous solar activity and space weather prediction [16-19].

The X-ray fluxes themselves are of little use for quantitative physical understanding of processes in the Sun's atmosphere. However, the temperature and emission measurements of the plasma produced by soft X-rays are mirrored, and these physical quantities are of great importance: the energy of solar flares and other energy releases can be deduced from them.

Corresponding volume emission measure of the solar soft X-ray emitting plasma observed by the GOES/XRS. The volume emission measure were obtained in SunPY using the methods of White et al. [20] who used the CHIANTI atomic physics database to model the response of the ratio of the short (0.5-4 angstrom) to long (1-8 angstrom) channels of the XRSs onboard various GOES satellites. Obtained histogram of the data of a map is shown in Figure 4.

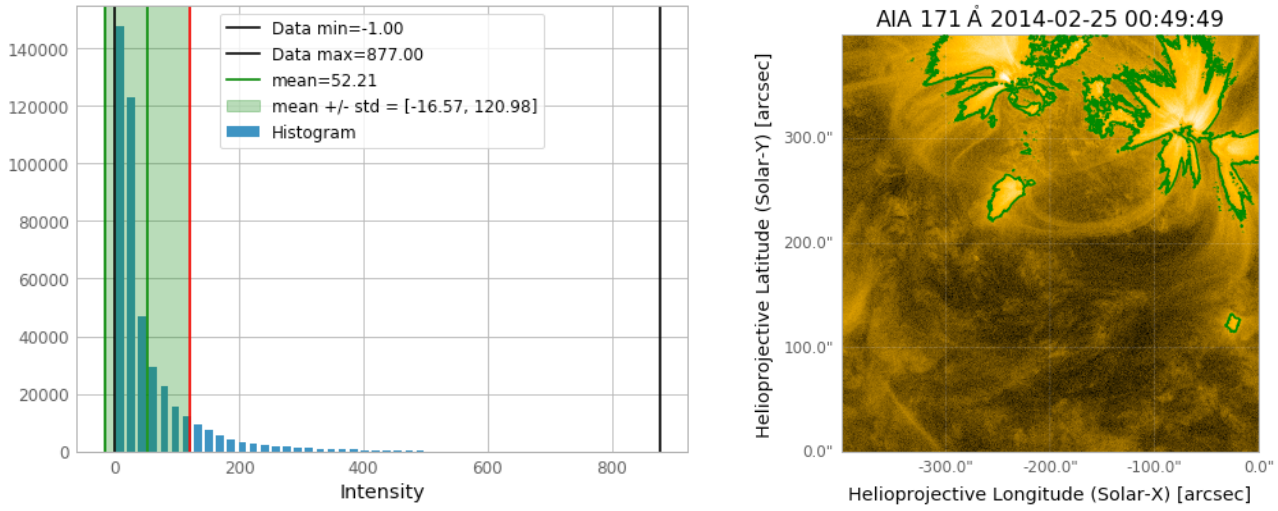

Figure 4 – Obtained histogram of the data of a map.

3. Conclusions

In other disciplines, the scientific python culture is much more developed than in solar physics. SunPy is making use of existing scientific python projects, with potential future deeper integration with projects such as Astropy and sci-kit image. Using SunPy package we have obtained the values of temperature and emission measure from a GOES Light Curve. This function calculates the isothermal temperature and corresponding volume emission measure of the solar soft X-ray emitting plasma observed by the GOES/XRS.

Acknowledgments

This work was partly supported by the Asian Research Center Foundation for Research program in National University of Mongolia.

References

1 Gyenge N., Ballai I., Baranyi T. Statistical study of spatio-temporal distribution of precursor solar flares associated with major flares // Monthly Notices of the Royal Astronomical Society. – 2016. – Vol. 459. –No.4. – P. 3532 – 3539.

2 Svestka, Z., Cliver, E.W. Eruptive sol. Flares // Lecture Notes in Physics. -1992. – Vol. 399. -P. 1.

3 Haisch, B., Strong, K.T., Rodono, M. Flares on the Sun and other stars // Ann. Revs. Astron. Astrophys. – 1991. – Vol. 29. – P. 275.

4 Feldman, U., Laming, J.M., Doschek, G.A. The correlation of Sol. flare temp. and EM extrapolated to the case of stellar flares // Astrophys. J. Lett. – 1995. –Vol. 451. – P.79.

5 Shimizu T. Energetics and occurrence rate of active-region transient brightenings and implications for the heating of the active-region Cor. // Publ. Astron. Soc. Japan. – 1995. – Vol.47. – P. 251–263.

6 http://www.ngdc.noaa.gov/stp/satellite/goes/

7 ftp://ftp.ngdc.noaa.gov/STP/space-weather/solar-data/solar-features/solar-flares/x-rays/goes/

8 Mumford S.J., Christe S. SunPy-Python for solar physics //Comput. Sci. Disc. – 2015. –Vol.8. – P. 014009.

9 Garcia H.A. Reconstructing the thermal and spatial form of a solar flare from scaling laws and soft X-Ray measurements // ApJ. – 1998. – Vol.504. – P.1051.

10 Tsuneta S., Masuda S., Kosugi T., Sato J. Hot and superhot plasmas above an impulsive flare loop // ApJ. – 1997. – Vol.478. – P.787.

11 Isobe H., Yokoyama T., Shimojo M., Morimoto T., Kozu H., Eto S., Narukage N., Shibata K. Reconnection rate in the decay phase of a long duration event flare on 1997 May 12 // ApJ. – 2002. – Vol.566. – P.528.

12 Isobe H., Takasaki H., Shibata K. Measurement of the energy release rate and the reconnection rate in solar flares // ApJ. – 2005. – Vol.632. – P.1184.

13 Sweet P.A. Electromagnetic phenomena in cosmical physics // Cambridge Univ. Press. – 1958. – 123 p.

14 Spitzer L. Physics of Fully Ionized Gases //Interscience. – 1956.

15 Sarsembayeva, A. T., Sarsembay, A. T. Solar activity monitoring for the period April 10-20, 2017 // News of the National Academy of Sciences of the Republic of Kazakhstan-series Physico-Mathematical. – 2018. – Vol.2 . –No.318. – P.9-11.

16 Aschwanden M. J., Alexander D. Solar flare and CME observations with STEREO/EUVI // Solar Phys. – 2001. – Vol.204. – P.91.

17 Bornmann P.L. Limits to derived flare properties using estimates for the background fluxes-Examples from GOES // Astrophys. – 1990. – Vol. J356. – P.733.

18 Phillips K. J.H., Feldman U. Properties of cool flare with GOES class B5 to C2 // Astron. Astrophys. – 1995. – Vol.304. – P.563.

19 Garcia H. A. Forecasting methods for occurrence and magnitude of proton storms with solar hard X rays // Space Weather. – 2004. – Vol.2. – P.S06003.

20 White S.M., Thomas R.J., Schwartz R.A. Updated expressions for determining temperatures and emission measures from goes soft X-Ray measurements // Solar Physics. – 2005. Vol.227. – P.231.

IRSTI 29.19.11 https://doi.org/10.26577/phst.2020.v7.i2.04

Influence of Al and Mn impurities on structural processes transformations in copper alloys

V.A. Lobodyuk[1], K.M. Mukashev[2,*] and D.E. Tolen[2]

[1]*G. V. Kurdyumov Institute for Metal Physics of the N.A.S. of Ukraine, 36, Academician Vernadsky Boulevard, UA-03142 Kyiv, Ukraine*
[2] *Bashkir State University, 32, Zaki Validi St.,, Ufa, Bashkortostan, Russia*
[*]*e-mail: mukashev.kms@gmail.com*

In the work on specific examples involving real copper-based alloys containing 14 weight.%Al and 3 weight.%Mn, describes the results of a study of the process of restoring the shape of a material that was defomated according to the three-point bending scheme. The studies were carried out by measuring changes in the temperature dependence of the electrical resistance and deflection of the sample, as well as by obtaining microelectronograms using an electron microscope. Since SME alloys operate under conditions of mandatory thermal cycling, the elucidation of the thermal stability of these materials is of practical interest. It is established that martensitic crystals that occur in hardened samples have a high density of packing defects and thin twins formed on the (121) γ′ plane. One of the important features of the martensitic mechanism is the obligatory formation of martensite with defects, which is a fine structure. By comparing the curves of the electrical resistivity and the deflection, it was found that the temperature range of the increase in the deflection upon cooling coincides with the temperature range of the direct martensitic transformation. In addition to stacking faults, thin twins with a thickness of 0.01-0.04 microns are also observed in martensite crystals. It was found in the analysis that twinning in martensite occurs along the {121} γ′ plane. It is shown that the streakiness arising during martensitic transformations is caused by stacking faults, which lie in the {121} plane at a high density of stacking faults.

Keywords: metals, alloys, martensite, electrical resistance, electron microscopy, structure, alloying.
PACS numbers: **61.66.Dk, 81.30.Bx.**

1 Introduction

The phenomenon of thermoelastic martensitic transformation predicted at the time by G. V. Kurdyumov and later discovered on CuAlNi alloys these results have led to the appearance of many works devoted to the study of various aspects of this unique phenomenon. The most interesting and of great scientific and applied significance are the shape memory effect (SME), superelasticity, and two-way (reversible) shape memory [1,2]. The essence of the shape memory effect is as follows. Loading a material sample in the temperature range of martensitic transformation leads to its deformation in the form of stretching, bending, etc. This deformation can be «removed» by heating above the temperature of the end of the reverse transformation. In this case, the sample is deformed due to the directed growth of martensitic crystals under the action of applied stresses [5]. A similar process is observed in all materials that undergo reversible martensitic transformation. The difference can only be in the degree of restoration of the original form that existed before the transformation. It should be noted that in alloys with thermoelastic martensitic transformation, the original shape is completely restored. In materials with a large hysteresis of the forward-reverse transformation process, a partial restoration of the original shape is observed, as a result of which part of the deformation obtained during cooling under load is preserved [3,4].

Since then, a significant number of works have been performed on the study of the phenomenon associated with martensitic transformation. However, there are a number of problems that have not yet been solved, including the lack of consensus on the conditions for the existence of a complete restoration of the original shape when the material is heated after deformation[10].

Determining these conditions is extremely important when choosing materials with SME used in devices designed to solve various structural and multifunctional tasks. Let us briefly explain the essence of martensitic transformation [7, 9].

Martensitic transformation is a subspecies of polymorphic transformation in which the relative positions of the atoms that make up the crystal are changed by their ordered movement. In this case, the relative displacements of neighboring atoms are small compared to the interatomic distance [6, 11]. The rearrangement of the crystal lattice in microblasts is usually reduced to the deformation of its cell, and the final phase of the martensitic transformation can be considered as a uniformly deformed initial phase [8, 12]. The strain value is small (about 1-10%) and correspondingly small compared to the binding energy in the crystal. The microstructure of martensite has a needle-like (plate-like) or rack-and-pinion (batch) appearance. It can be observed in hardened metal alloys and in some pure metals that are characterized by polymorphism. Martensite is the main structural component of hardened steel. For steel, it is an ordered supersaturated solid solution of carbon in α-iron of the same concentration as the original austenite [17]. The memory effect of metals and alloys is associated with the transformation of martensite during heating and cooling. It received its name in honor of the German metal scientist Adolf Martens, whose name is associated with the discovery of this phenomenon [14, 15, 20].

One of the important features of the martensitic mechanism is the mandatory formation of martensite with defects, which is a thin structure [16, 19]. The latter has a certain effect on a number of properties of materials, including hardening and SME parameters. By changing the concentration of one of the elements in the alloy, you can get martensite with different substructures with the same mechanical properties of the entire system. In addition, since SME alloys operate under conditions of mandatory thermal Cycling, the determination of the thermal stability of these materials is of important practical interest. In this regard, this article will review some experimental results of the study of SME in cases where the martensite transformation proceeds with different hysteresis, and the martensite itself has a different fine structure [13, 18, 21].

2 Fine structure of martensite and memory effect in a copper-based alloy

To study the shape recovery during the reverse transformation, the alloy samples were prepared in the following composition: Cu+14 weight.% Al+3weight.%Mn with Mn = 10oC. The samples were deformed according to the three-point bending scheme. Loading was performed above the Aκ point [6]. the Load was selected in such a way that the maximum stresses arising in the sample were significantly lower than the yield strength of the high-temperature β1 phase. When cooling in a certain temperature range, the deflection of the sample increases sharply (Figure1b). A comparison of the electrical resistance curves (Figure 1a) and the deflection curve (Figure 1b) shows that the temperature range of increasing deflection during cooling coincides with the temperature range of direct martensitic transformation.

After the load is removed at the temperature of liquid nitrogen, the shape is restored during heating in the interval of reverse martensitic transformation (Figure 1 a, b). If the maximum stresses applied before loading do not exceed the yield strength, then complete straightening during heating is observed even if the sample is not unloaded before heating and it, unbending, performs work against an external force. In this case, the interval of the mold recovery temperature is slightly shifted towards higher temperatures compared to the case when the load does not prevent the mold recovery. It should be noted that the curves of the temperature dependence of the electrical resistance when heated under load remain almost unchanged. This is probably because the amount of martensitic phase that causes the shape change is at the level of the sensitivity threshold of the resistometric technique. Complete restoration of the original shape during heating was also observed after plastic deformation at -196oC. However, in this case, to obtain the same residual deflection as when cooling under load, loads 10-15 times greater are required.

During the quenching process in the studied alloy, the initial β – phase is ordered and a β1-phase is formed with a parameter 2 times greater than the parameter of the β – phase. Microelectronograms from the ordered β1 phase show superstructural reflexes, while micrographs show curved antiphase boundaries (Figure 2). A certain amount of martensitic crystals is preserved in the samples at room temperature. the γ-phase is also ordered, but the antiphase domains in martensite are smaller than in the initial phase.

Martensitic crystals that occur in hardened samples most often consist of two halves separated by a median plane. In each half of the crystal, banding is observed, which leads to the appearance of strands on microelectronograms obtained from such sites.

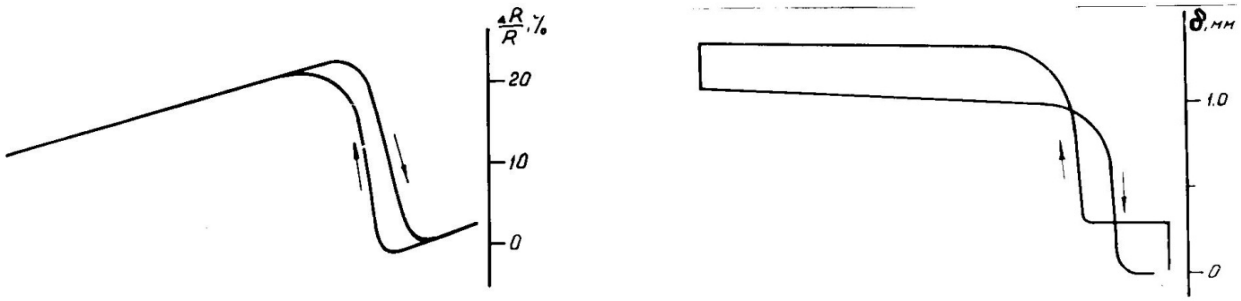

a) b)

Figure 1 – Temperature dependences of electrical resistivity (ΔR/R) and deflection (δ) of CuAlMn alloy

Figure 2 – Antiphase boundaries in the β1 phase of CuAlMn alloy

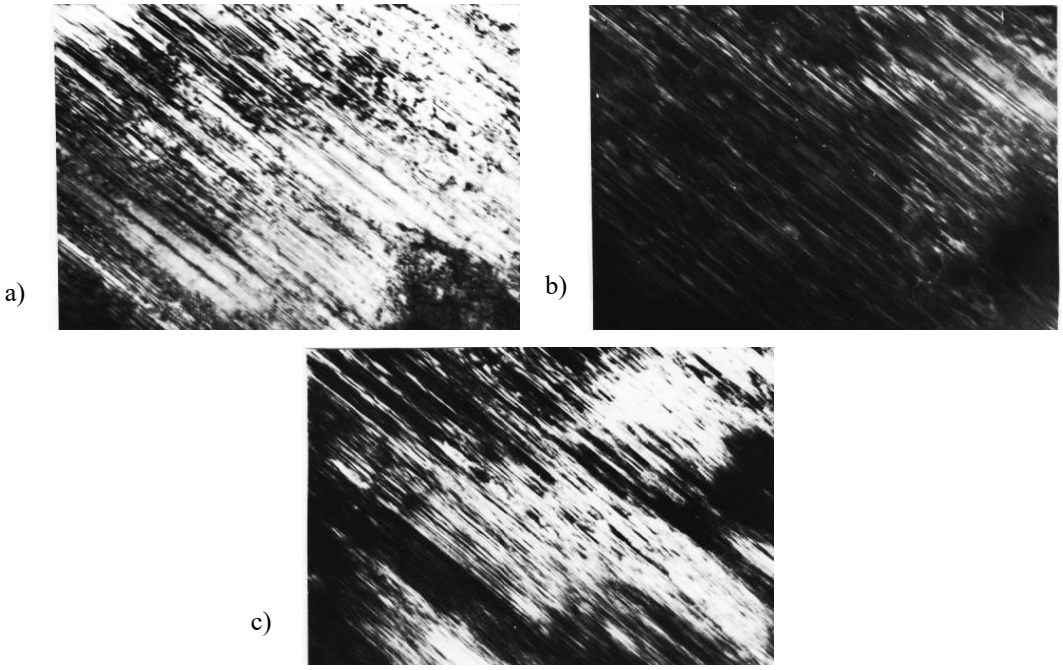

a) b) c)

Figure 3 – Section of a Martensitic cualmn alloy crystal with packaging defects: a) light field image; b) reflection in the reflex (100)γ′; c) image in the reflex (200)γ′.

The strands are always perpendicular to the banding in micrographs. Banding is caused by packaging defects that lie in the {121} plane. The density of packaging defects is quite high. Figure 3 shows micrographs of a section of a martensitic crystal with banding in a light and dark field.

In addition to packing defects, thin twins with a thickness of 0.01-0.04 microns are also observed in martensitic crystals. During the analysis, it was found that twinning in martensite occurs along the {121}γ′ plane. A micrograph of a section of a martensitic crystal with thin twins is shown in Fig.4. Within the broader twin plots was also observed in the banding caused by defective packaging. In the initial β1 phase after quenching, the dislocation density is low, and only single dislocations are observed. After β1 → γ′ transformation, areas with high dislocation density were also found in martensitic crystals.

In addition to thin twins, relatively wide (up to 1 mm) twin sections were found in the γ′ – phase. The borders of such doubles are usually straight. These twins could be formed due to the stresses that occur during the martensitic transformation (observed after the end of β1 → γ′ upreversion at a given temperature) or as a result of the appearance of local thermal stresses in thin films when viewed in an electron microscope (the twins were formed during observation).

The direction of banding changes in the foreground areas (Figure 5). It was found that in this case, too, the twinning occurs along the {121} γ′ plane.

When cooled, martensitic crystals or plates are formed with both smooth and jagged borders (Figure 6). Compression deformation (2%) leads to the appearance of martensite plates with banding and reoriented sections with a width of approximately (0.2-0.4) microns. The boundaries of these sections are located in the {121}γ′ and {101}γ′ planes. In some areas, the density of dislocations in martensite increases. It should be noted that after deformation, martensitic crystals with jagged interfacial boundaries appear more often.

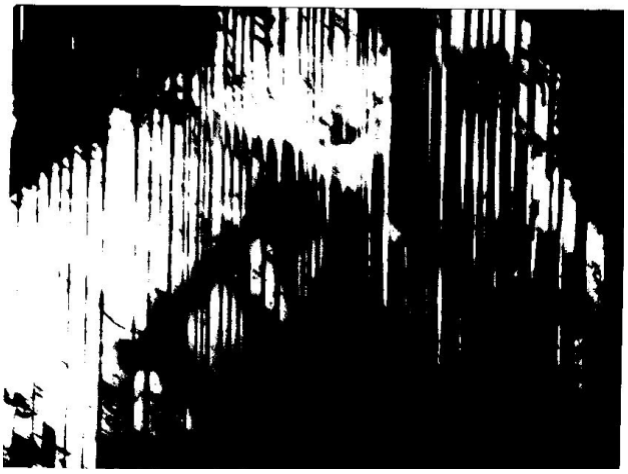

Figure 4 – Thin twins in the γ-phase of the CuAlMn alloy at the orientation [111]

Figure 5 – Twin sections of the CuAlMn alloy in the γ-phase with the orientation [010]

3 Conclusions

Studies of the influence of al and Mn impurities on the processes of structural transformations in copper alloys subjected to plastic deformation according to the three-point bending scheme by measuring the temperature dependence of electrical resistance have shown that this dependence is practically unchanged. The main reason for this process is probably that the concentration of the martensitic phase formed in the alloy as a result of plastic deformation does not exceed the sensitivity threshold of the method based on the measurement of electrical resistance. However, if the load acting on the sample is increased by more than 10 times at a temperature of – 196oC, it is possible to achieve complete restoration of the original shape of the material. According to electron microscopic studies, the main structural disorders that occur in this case are defects in high-density packaging and thin twins, the dimensions of which do not exceed 0.01-0.04 microns in thickness. It is established that the predominant formation of the latter occurs on the plane (121) γ′.

a) b)

Figure 6 – CuAlMn martensitic crystals with smooth (a) and jagged (b) borders

References

1 Kurdyumov G. V. Yavleniya zakalki i otpuska stali, Moscow, 1960. 64 p. (in Russian).

2 Pilyugin V.P., Pacelov A.M., Degtyarev M.V. et. al. Vliyanie predvaritelnoj deformacii austenita v zhelezonikelevom splave na martensitnoe prevrashenie pri ohlazhdenii // Fizika metallov i metallovedenie. -2012. -Vol.113.-No.7, -P.711–721. (in Russian).

3 Bojko V.S., Garber R.I., Kosevich A.M. Obratimaya plastichnost kristallov. – Nauka, Moscow. 1991. – 280 p. (in Russian).

4 Lobodyuk V.A., Estrin E.I. Izotermicheskoe martensitnoe prevrashenie // UFN. – 2005. –Vol. 175. –No. 7. – P. 745–765. (in Russian).

5 Zotov O.G., Kiselnikov V.V., Kondratev S.Yu. Fizicheskoe metallovedenie. SPBGTU, Saint-Petersburg, -2001. 266 p. (in Russian).

6 Lobodyuk V.A., Estrin E.I. Martensitnye prevrasheniya. Fizmatlit, Moscow. -2009, 352 p. (in Russian).

7 Singh S. et al. Microstructural analysis and tribological behavior of aluminum alloy reinforced with hybrid alumina/nanographite particles // Journal of Engineering Tribology. – 2015. -Vol. 229. – No. 5. -P. 597–608.

8 Sittner P., Novak V. Anisotropy of martensitic transformations in modeling of shape memory alloy polycrystals // I International Journal of Plasticity. – 2000. – Vol.16.- P. 1243-1268.

9 Wayman C.M., Shimizu K. The shape memory (marmem) effect in alloys // Metallurgical Science. -1972. -Vol. 6. –No. 10. – P. 175-183.

10 Otsuka K., Wayman C.M. Mechanism of shape memory effect and superelasticity // Shape memory materials., eds. Otsuka K. and Wayman C.M. Cambridge University Press, Cambridge. 1998. – P. 27-48.

11 Otsuka K. Martensitic transformation in nonferrous shape memory alloys // J.Materials Science and Engin. -1999. –Vol. A273-275. – P.89-105.

12 Culshaw B. Smart structures and materials. – Boston: Artech House. 1996. – P. 207.

13 Kornilov I. I., Belousov O. K., Kachur E. V. Titanium nickelide and other alloys with the «memory» effect. Nauka, Moscow, 1977. – 161 p.

14 Perkins D. Thermomechanical characteristics of alloys with thermoelastic martensite. The shape memory effect in alloys / D. Perkins, G. R. Evards, S. R. Sach [et al.]. Metallurgy, Moscow, 1979. – PP. 230-254.

15 Khachin V. N. Martensitic inelasticity of alloys / / Izvestiya vuzov. Physics. – 1985. –No. 5. – PP. 82-103. (In Russian).

16 Culshaw B. Smart structures and materials. Artech House, Boston, 1996. – P. 207.

17 Volchenko D. A. Alloys with shape memory / / Automotive industry. -1991. –No. 8. – P. 30-31.

18 Boyko V. S., Garber R. I., Kosevich A.M. Reversible plasticity of crystals. Phys.-math. lit., Moscow, 1991, 280 p.

19 Shishkin S. V., Makhutov N. A. Calculation and design of power structures on alloys with shape memory effect. Izhevsk, «Regular and chaotic dynamics», 2007. 412 p. (In Russian).

20 Duerig T.W. et al. Engineering aspects of shape memory alloys. Butterworth-Heinemann, London, 1990. 394 p.

21 Wei Z.G., Sandström R., Miyazaki S. Review. Shape memory materials and hybrid composites for smart systems. Part I. Shape memory materials. Part II. Shape memory hybrid composites // Journal of Materials Science. – 1998. – Vol. 33. – P. 3743-3783.

IRSTI 58.33.09 https://doi.org/10.26577/phst.2020.v7.i2.05

Study of structural changes in ZrO_2 ceramics irradiated with heavy ions of Kr^{15+} with an energy of 147 MeV.

M.Alin[1] and A.L. Kozlovskiy[1,2]

[1]*L.N. Gumilyov Eurasian National University, 010008, Nur-Sultan, Kazakhstan*
[2]*Laboratory of Solid State Physics, Institute of Nuclear Physics, 050032, Almaty Kazakhstan*
**e-mail: kozlovskiy.a@inp.kz*

This paper presents the results of a study of changes in structural characteristics, such as the degree of crystallinity, dislocation density, and deformation of the crystal lattice in ZrO_2 ceramics as a result of irradiation with heavy Kr^{15+} ions with an energy of 147 MeV. The choice of the type of irradiation ions is due to the possibility of simulating the processes of defect formation comparable to the irradiation of radiation-resistant materials by fragments of uranium fission. The radiation doses ranged from $5x10^{13}$ to $1x10^{16}$ ion/cm^2. The dependences of the change in the crystallographic parameters on the radiation dose were established. At the same time, the maximum decrease for an irradiation dose of $1x10^{16}$ ion/cm^2 was no more than 10 %, which in turn indicates a high radiation resistance to the accumulation of defects during large-dose irradiation. It was determined that the greatest change in the degree of crystallinity is observed above a dose of $1x10^{15}$ ion/cm^2. The data obtained indicate a high degree of resistance of these ceramics to radiation damage.

Key words: heavy ions, ZrO_2 ceramics, radiation-resistant ceramics, new structural materials.
PACS numbers: 25.85.Ec, 28.41.Fr

1 Introduction

To date, the most promising materials for nuclear power as structural materials are oxide or nitride ceramics, which are highly resistant to degradation, refractory and wear resistance, and good insulating properties [1-5]. Among the variety of oxide types of ceramics, one can distinguish ceramics based on zirconium dioxide (ZrO_2), which are among the most refractory oxides (T_{melt}=2715°C). In nature, zirconium dioxide exists in three crystalline forms: in the form of a monoclinic structure characteristic of the mineral baddeleyite, a metastable tetragonal phase, and an unstable high-temperature cubic phase [5-15]. Resistance to most types of acids and alkalis, as well as high wear resistance and refractoriness make ceramics based on ZrO_2 the basis for the manufacture of refractory, abrasive materials, superhard glasses and fuel cells [16,17]. All of the above properties make ZrO_2-based ceramics one of the candidate materials as the basis for the materials of the first wall of high-temperature reactors. However, in the case of potential application of ZrO_2 ceramics in this direction, it is necessary to know the degree of resistance of these ceramics to the action of ionizing radiation, as well as the effect of the accumulation of structural defects in the material [18-20].

The aim of this work is to study the structural changes in ZrO_2 ceramics as a result of irradiation with heavy Kr^{15+} ions with an energy of 147 MeV.

2 Experimental technique

Commercial samples of ceramics based on zirconium dioxide with a tetragonal type of crystal lattice were selected as objects of research. The choice of these ceramics as an object of research is due to their high resistance to chemical and temperature degradation, as well as their increased resistance to radiation damage [21-25].

The irradiation of ceramics was carried out on a DC-60 heavy ion accelerator. The ions for irradiation were Kr^{15+} ions with an energy of 147 MeV. The radiation doses ranged from $5x10^{13}$ to $1x10^{16}$ ion/cm^2. The choice of the type of irradiation ions is due to the possibility of simulating defect formation processes in the range of particle energies comparable to irradiation with uranium fission fragments in a reactor. The choice of the range of irradiation doses is due to the possibility of simulating defect formation processes both in the case of the begin-

ning of the overlapping of ion trajectories in the material, and in the case when the probability of overlap exceeds 1000.

The study of the effect of irradiation on structural distortions and amorphization as a result of the accumulation of defects in the irradiated material was carried out using the standard method of X-ray diffraction, which belongs to the methods of non-destructive testing of defects. The studies were carried out using X-ray diffraction of the samples in the angular range 2θ=20-100°, with a step of 0.03°. X-ray diffraction patterns were recorded on a D8 Advance ECO powder X-ray diffractometer, Bruker, Germany. The assessment of changes in structural characteristics was carried out by determining changes in the shape and intensity of diffraction lines, as well as their distortion.

3 Discussion

Figure 1 shows the dynamics of changes in the X-ray diffraction patterns of the studied ceramics before and after irradiation. The general view of the diffraction patterns indicates a polycrystalline structure of ceramics with a high degree of structural ordering, which is evidenced by the symmetric shape of the diffraction lines in the diffraction pattern of the initial sample. The general view and angular position of the diffraction peaks are characteristic of the tetragonal phase of zirconium oxide with the spatial symmetry P42/nmc (137), which is most common for this type of ceramics.

For irradiated samples, according to the given X-ray diffraction data, the appearance of new reflections was not detected, which indicates the absence of phase transformation processes or the formation of new phase inclusions as a result of the accumulation of defects in the structure.

The main changes in the diffraction patterns are reflected in the form of changes in the shape of the diffraction peaks, as well as their intensity. These changes indicate that the main structural changes in this case are associated with deformation and disordering of the crystal structure, changes in dislocation density, and the formation of highly disordered regions or amorphous-like inclusions in the structure. These changes are caused by the processes of defect formation, which arise as a result of elastic and inelastic collisions of incident ions with atoms of the crystal lattice, as well as the formation of displacement atoms and knocked out electrons. In this case, in the case of irradiation with high-energy ions with an energy of more than 100 MeV, the main contribution to the energy losses of incident ions is made by elastic collisions of ions with electron shells, as a result of which cascades of knocked-out electrons arise and, therefore, the electron density in the irradiated material changes.

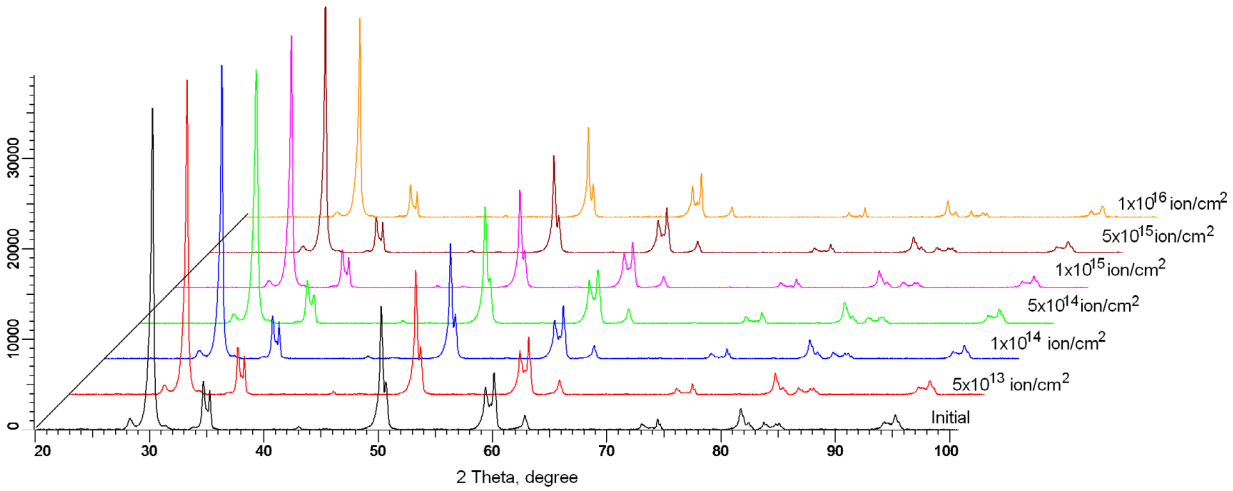

Figure 1 – X-ray diffraction patterns of ceramics before and after irradiation

Analyzing the obtained data of X-ray diffraction patterns, it was found that the greatest changes in the shape of diffraction peaks are observed at irradiation doses above $1x10^{15}$ ions/cm^2, which are characterized by an increase in the overlapping areas of defects by more than 100 times. As is known, in the case of single ion trajectories isolated from each other in the material, most of the formed point defects are

capable of annihilating with each other, thereby not making a significant contribution to the change in the concentration of defects in the ceramic material. However, in the case when the trajectories of incident ions begin to overlap, which is observed with an increase in the radiation dose, the concentration of defects becomes much higher and can lead to the formation of regions of disorder and deformation of the crystal lattice in the structure. In the case of high-temperature refractory ceramics, the formation of defect regions can lead to a decrease in the degree of perfection of the crystal structure due to partial disordering and deformation. Figure 2 shows the dynamics of the dependence of the change in the degree of crystallinity of the studied ceramics as a result of irradiation.

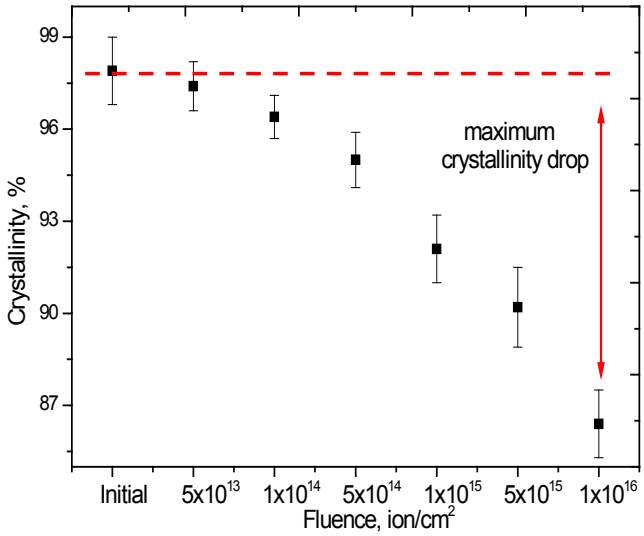

Figure 2 – Dynamics of changes in the degree of crystallinity of the studied ceramics as a result of irradiation

According to the data obtained, it can be seen that the greatest decrease in the degree of crystallinity is observed for samples irradiated with a dose of $1x10^{15}$ ion/cm^2 and above. At the same time, the maximum decrease for an irradiation dose of $1x10^{16}$ ion/cm^2 was no more than 10 %, which in turn indicates a high radiation resistance to the accumulation of defects during large-dose irradiation.

Based on the change in the shape and intensity of the diffraction peaks, the contributions from amorphous-like inclusions and highly disordered regions in the structure of ceramics, which appeared as a result of an increase in the radiation dose, were calculated. The calculation method was based on the approximation of diffraction peaks by the required number of pseudo-Voigt functions, which make it possible to separate the contribution from amorphous-like inclusions and an ordered structure. Figure 3 shows the results of these calculations.

As can be seen from the data presented, the change in the concentration of amorphous-like inclusions in the structure of ceramics as a result of an increase in the irradiation dose is nonlinear and has a pronounced increase in the samples irradiated with a dose above $1x10^{15}$ ion/cm^2. This nonlinearity of changes in the concentration of amorphous-like inclusions is due to an increase in the regions of overlapping ion trajectories in ceramics, as a result of which the defects do not have time to annihilate, but form cluster two-dimensional and three-dimensional defects. In this case, the formation of strongly disordered regions can lead to a strong deformation of the crystal lattice, which is also clearly seen from the asymmetric shape of the diffraction maxima for samples irradiated with high doses.

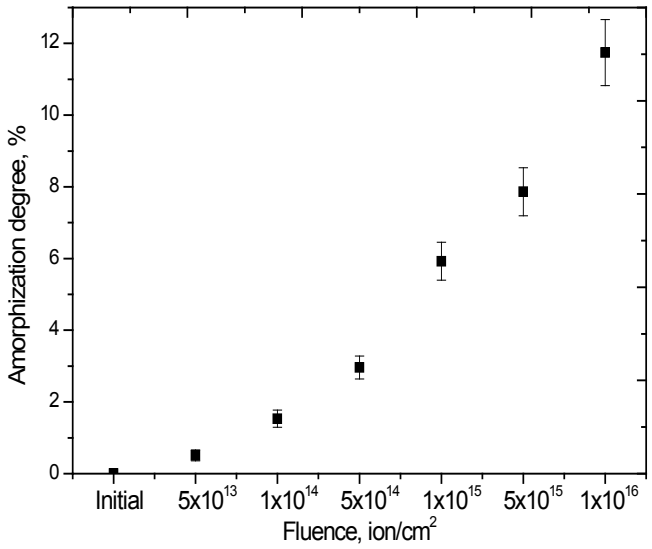

Figure 3 – Graph of the dependence of the change in the concentration of amorphous-like inclusions in the structure of ceramics as a result of an increase in the radiation dose

4 Conclusions

In conclusion, the studied ZrO_2 ceramics have a high degree of resistance to radiation damage under high dose irradiation, and the maximum degree of disordering and amorphization of the structure at high irradiation doses of $1x10^{15}$ – $1x10^{16}$ ion/cm^2 is no more than 7-12 %. At the same time, no new phase inclusions or impurity formations were observed for all irradiated samples, which also indicates the high resistance of these ceramics not only to radiation damage, but also to phase transformations that can occur during large-dose irradiation.

References

1 Liu J. et al. In-situ TEM study of irradiation-induced damage mechanisms in monoclinic-ZrO_2 // Acta Materialia. – 2020. – Vol. 199. – P. 429-442.

2 Chauhan V., Kumar R. Phase transformation and modifications in high-k ZrO_2 nanocrystalline thin films by low energy Kr^{5+} ion beam irradiation // Materials Chemistry and Physics. – 2020. – Vol. 240. – P. 122127.

3 Wang Z. G. et al. Enhanced nucleation undercooling and surface self-nanocrystallization of Al_2O_3-ZrO_2 (Y_2O_3) eutectic ceramics // Journal of the European Ceramic Society. – 2019. – Vol. 39. –No.4. – P. 1707-1711.

4 Wang J. et al. Pump laser induced photodarkening in ZrO_2-doped Yb: Y_2O_3 laser ceramics // Journal of the European Ceramic Society. – 2019. – Vol. 39. –No.2-3. – P. 635-640.

5 Kadyrzhanov K. K., Tinishbaeva K., Uglov V. V. Investigation of the effect of exposure to heavy Xe22+ ions on the mechanical properties of carbide ceramics // Eurasian Phys. Techn. J. – 2020. – Vol. 17. –No.33. – P. 46-53.

6 Peuchert U. et al. Transparent cubic-ZrO2 ceramics for application as optical lenses //Journal of the European Ceramic Society. – 2009. – Vol. 29. – No. 2. – P. 283-291.

7 Deng Z. Y. et al. Microstructure and thermal conductivity of porous ZrO_2 ceramics //Acta materialia. – 2007. – Vol. 55. – No. 11. – P. 3663-3669.

8 Han J. et al. Highly porous ZrO_2 ceramics fabricated by a camphene-based freeze-casting route: Microstructure and properties //Journal of the European Ceramic Society. – 2010. – Vol. 30. – No. 1. – P. 53-60.

9 Li W. et al. Preparation, microstructure and mechanical properties of ZrB2–ZrO2 ceramics //Journal of the European Ceramic Society. – 2009. – Vol. 29. – No. 4. – P. 779-786.

10 Zhang K. et al. Digital light processing of 3Y-TZP strengthened ZrO_2 ceramics //Materials Science and Engineering: A. – 2020. – Vol. 774. – P. 138768.

11 Liu Y. et al. Fabrication of micro-scale textured grooves on green ZrO_2 ceramics by pulsed laser ablation //Ceramics International. – 2017. – Vol. 43. – No. 8. – P. 6519-6531.

12 Rittidech A., Somrit R., Tunkasiri T. Effect of adding Y_2O_3 on structural and mechanical properties of Al2O3–ZrO2 ceramics //Ceramics international. – 2013. – Vol. 39. – P. S433-S436.

13 He S., Tong H., Liu G. Spark assisted chemical engraving (SACE) mechanism on ZrO2 ceramics by analyzing processed products //Ceramics International. – 2018. – Vol. 44. – No. 7. – P. 7967-7971.

14 Guo L., Li M., Ye F. Phase stability and thermal conductivity of RE2O3 (RE= La, Nd, Gd, Yb) and Yb2O3 co-doped Y2O3 stabilized ZrO2 ceramics //Ceramics International. – 2016. – Vol. 42. – No. 6. – P. 7360-7365.

15 Santa Cruz H., Spino J., Grathwohl G. Nanocrystalline ZrO2 ceramics with idealized macropores //Journal of the European Ceramic Society. – 2008. – Vol. 28. – №. 9. – P. 1783-1791.

16 Ivanov K. V., Kalashnikov M. P. Structure and phase composition of "ZrO_2 thin coating–aluminum substrate" system processed through pulsed electron beam irradiation // Applied Surface Science. – 2020. – Vol. 534. – P. 147628.

17 Baksht E. K. et al. Yttrium sesquioxide ceramics glow under irradiation with an electron beam // Russian Physics Journal. – 2020. – P. 1-7.

18 Srivastava S. K. et al. Ionoluminescence to study irradiation stability of zirconia // AIP Conference Proceedings. – AIP Publishing LLC, 2020. – Vol. 2265. -No.1. – P. 030225.

19 Xia W. et al. Corrosion behavior of a sol-gel ZrO_2 pore-sealing film prepared on a micro-arc oxidized aluminum alloy //Ceramics International. – 2019. – Vol. 45. –No. 8. – P. 11062-11067.

20 Leonov A. A. et al. Effect of electron beam irradiation on structural phase transformations of zirconia-based composite reinforced by alumina nanofibers and carbon nanotubes // Journal of Physics: Conference Series. – IOP Publishing. – 2019. – Vol. 1393. –No. 1. – P. 012106.

21 Börner F. D., Lippmann W., Hurtado A. Laser-joined Al_2O_3 and ZrO_2 ceramics for high-temperature applications //Journal of nuclear materials. – 2010. – Vol. 405. – No. 1. – P. 1-8.

22 Guo H. et al. Cold sintering process for 8 mol% Y2O3-stabilized ZrO_2 ceramics //Journal of the European Ceramic Society. – 2017. – Vol. 37. – №. 5. – P. 2303-2308.

23 Yang Z. et al. Investigation of surface topography formation mechanism based on abrasive-workpiece contact rate model in tangential ultrasonic vibration-assisted CBN grinding of ZrO_2 ceramics //International Journal of Mechanical Sciences. – 2019. – Vol. 155. – P. 66-82.

24 Smirnov A., Bartolomé J. F. Microstructure and mechanical properties of ZrO_2 ceramics toughened by 5–20 vol% Ta metallic particles fabricated by pressureless sintering //Ceramics International. – 2014. – Vol. 40. – No. 1. – P. 1829-1834.

25 Bian R. et al. Experimental investigation on ductile mode micro-milling of ZrO_2 ceramics with diamond-coated end mills // Micromachines. – 2018. – Vol. 9. – No. 3. – P. 127.

IRSTI 29.05.03 https://doi.org/10.26577/phst.2020.v7.i2.06

Current and capacitance hysteresis in porous semiconductor nanofilms

Z.Zh. Zhanabaev, D.A. Turlykozhayeva*, S.B. Ikramova,
A.O. Tileu, A.A. Maksutova, B.A. Khaniyev, A.K. Khaniyeva

Department of Solid State Physics and Nonlinear Physics, Al-Farabi Kazakh National University,
71 al-Farabi Avenue, 050040, Almaty, Kazakhstan
e-mail: Dana.Turlykozhayeva@kaznu.kz

At present, the study of complex electro-physical characteristics of semiconductor nanofilaments and nanofilms is of interest: the presence of non-monotonic oscillating characteristics with memory, areas of negative differential resistance. The aim of this work is to experimentally study both the volt-ampere and volt-farad characteristics of semiconductor nanoporous structures. The studied samples of porous silicon with the p-n structure were obtained by electrochemical etching. Single-crystal silicon with a p – n+ junction was used as the initial substrate. The NI EL VIS II+ educational platform and the Agilent E4980A instrument were used to study the electrophysical characteristics. To measure the dependence of current on voltage, as well as capacitance on voltage, Inga contacts with a thickness of 370 nm each were applied to nanoporous films. Thus, in this work, the phenomena of current switching, hysteresis behavior of current, and capacitance of porous silicon nanofilms are experimentally studied. It was found that these effects are amplified by a factor of 3-4 when the films are irradiated with an infrared laser. The results of this work can be used in the field of nanotechnology to improve memory and sensory elements. The established experimental facts can serve as a basis for constructing physical theories.

Key words: Por-Si, Current-voltage characteristic, Volt-farad characteristic, Hysteresis
PACS numbers: 61.46.-w, 61.46.Km, 62.63.Hj, 73.63.-b.

1 Introduction

Porous silicon (por-Si) obtained by electrochemical anodizing has a wide range of unique properties and is a promising material for creating various new-generation devices [1-7]. It is known that por-Si can have a wide range of porosity (from 2 to 90%) depending on the conditions of electrochemical treatment, the level of doping with donor or acceptor impurities, the composition of the electrolyte, etc. It is obvious that por-Si with a specific pore volume of several percent and por-Si with the highest porosity inevitably differ from each other not only in structural but also in optical, luminescent, and electrical properties. The use of por-Si layers as active elements in these devices requires careful study of the electrical properties of this material.

In [8], current-controlled switching was observed in the p-type crystalline silicon (p-c-Si) / porous Si (PS) / hydrogenated amorphous n-type silicon (n-a-Si: H) heterostructure. The most noticeable characteristic of a sharp increase in current at a voltage of ~ 0.95 V with a direct measurement from 0 to 1.8 V and a sharp decrease at 0.78 V with a reverse measurement was obtained, forming a loop. It is noteworthy that both forward and reverse switching occurs at the same current value of 10.8 mA. A switching mechanism is proposed that takes into account the presence of trapped carriers at the silicon-nanocrystal-SiO_x interface. This is because parts of the captured charges were bound near the n-a-Si: H / PS and PS / p-c-Si interfaces, forming an additional Coulomb barrier for the main carriers. It was assumed that when a voltage is applied to the PS layer, the captured carriers destroy the barrier at a certain threshold value and promote switching.

In memory devices, generators, and fast switching devices, one of the important electrical characteristics is the negative differential resistance (NDR) – a local increase in the current [9]. NDR is observed in devices made of amorphous silicon/silicon carbide [10], Si/SiO_2 nanowires, and devices based on quantum dots [11], as well as in porous silicon [12,13]. In [14], the NDR was investigated for a Schottky diode made of porous silicon. It is shown that thin filaments in porous silicon have much lower electron mobil-

ity than thick filaments due to electron scattering on the surface. Some carriers can overcome the gap in the conduction band and flow into thin filaments. The negative differential resistance was due to the difference in the mobility of thick and thin wires in porous silicon.

In [15], we studied the performance characteristics of memristive devices depending on the annealing temperature of thin films of zinc oxide (ZnO) over porous silicon (PSi) in a two-layer configuration. Electrical characteristics demonstrated that the psi nanostructured substrate and the configuration of ZnO layers effectively contribute to an 8-fold increase in the memristive ratio. The effect of a single-layer ZnO-PS configuration with single and different annealing resulted in continuous and sudden switching. The tests revealed a decrease in the switching coefficient with an increase in the voltage step size.

The volt-Farad characteristic (CV) of porous silicon at room temperature is given in [16]. Very clear quasi-periodic oscillatory features were found at voltage values in the range from -50 V to 50 V. This is because the low-dimensional quantum restriction in the PC is a possible reason for the observed CV fluctuations at room temperature.

CV characteristics of carbon nanotubes deposited on layers of porous silicon were studied in [17]. CV curves taken using a frequency of 1 MHz and an RMS value of 20 mV showed that the capacitance decreases with increasing voltage. This decrease was non-exponential and the capacitance became constant at high voltages. This behavior has been observed and attributed to an increase in the depletion region, that is, an increase in the built-in voltage. The sample etched for 4 minutes had a negative capacity of about 5 V. Negative capacitance is related to the non-monotonic or positive behavior of the transient current derivative in response to a small voltage jump.

Memristive devices are made of nanostructured composites of porous silicon-metal oxide (ZnO and VO_2) [18, 19]. Electrical characteristics indicate that both devices have symmetrical zero-crossing hysteresis curves typical of memristive systems. Although both devices showed significant durability and stable switching coefficient, the ZnO-based device showed relatively better stability and a higher resistive switching coefficient of 86% compared to the VO_2-based device.

From a brief review, it should be concluded that the volt-ampere and volt-farad characteristics of semiconductor nanofilaments and nanofilms, as a rule, have non-monotonic oscillating curves with the presence of hysteresis loops and sections of negative differential resistance. However, universal approaches to describing processes on this issue have not yet been established. Currently, there is no general theory explaining the features of nonlinear electrical conductivity of nanocluster semiconductor films depending on their nanoscale structure.

The purpose of this work is to experimentally study the volt-ampere and volt-farad characteristics of semiconductor nanoporous structures and search for characteristic general patterns.

2 Materials and methods of work

Measurements of the current-voltage characteristics of porous silicon films were carried out on the Ni EL VIS II+ educational platform (figure 1), with and without exposure to 630 nm infrared laser films in the voltage range from 0 V to 2 V. This platform is competitive measuring equipment in the field of circuitry, control systems, and telecommunications.

Samples of porous silicon with a p-n structure and dimensions of 8 x 2 mm^2 were obtained by electrochemical etching. The etching time of the films was 3 min, and the current density was 50 mA / cm^2. As the initial substrate, the prepared monocrystalline silicon with the p-n^+ junction was used, where n^+ – layer diffusion is a gradient of the impurity of phosphorus with a concentration of main charge carriers 10^{19} cm^{-3} with a gradual decrease of the impurity to the boundary of the p-n junction. The thickness of the p-silicon was 350 microns with a resistivity of 10 Ohm×cm, and the thickness of the n-layer was about 500 nm. To remove phosphor silicate glass, the silicon surface was etched in a 10% solution of hydrofluoric acid and washed in isopropyl alcohol using an ultrasonic device, and then dried.

To study the dependence of electric current on voltage, as well as capacitance on voltage, Inga contacts with a thickness of 370 nm each were applied to nanoporous films.

The volt-farad characteristics of nanostructured and porous silicon samples were measured using an Agilent E4980A LCR meter (figure 2) under natural light and laser exposure in the voltage range from 0 V to 2 V and from 2 V to 0 V. The Agilent E4980A Precision LCR-Meter (figure 2) operates in the frequency range from 20 Hz to 2 MHz. The basic accuracy of the equipment is 0.05 %. The device has excellent reproducibility of measurements at low and high impedance values.

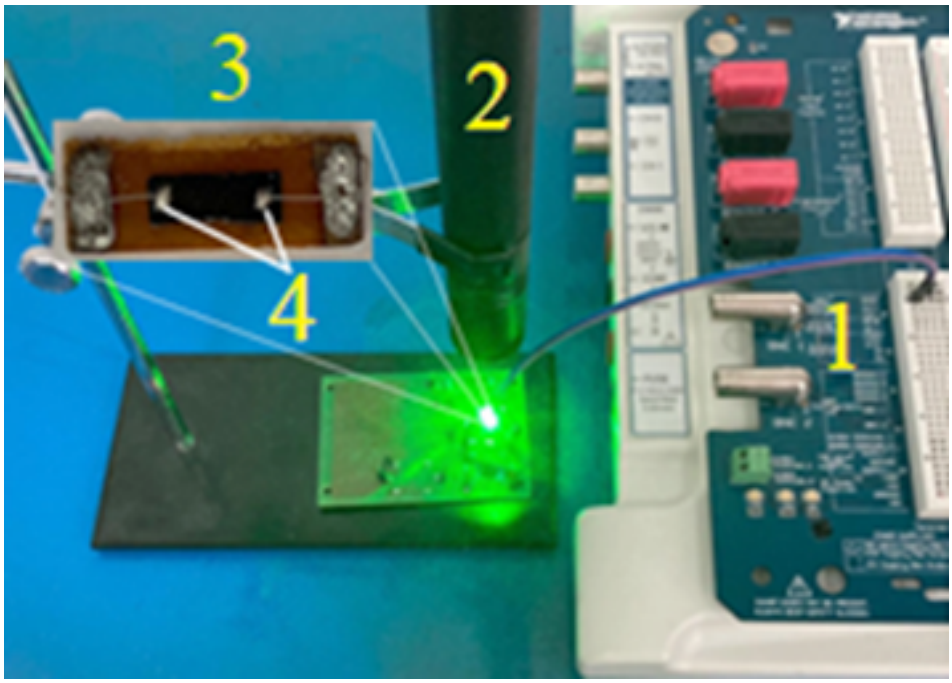

Figure 1 − Experimental setup: 1 – Ni EL VIS II + Platform,
2 − infrared laser, 3 – a porous silicon film, 4 − contact points on the film

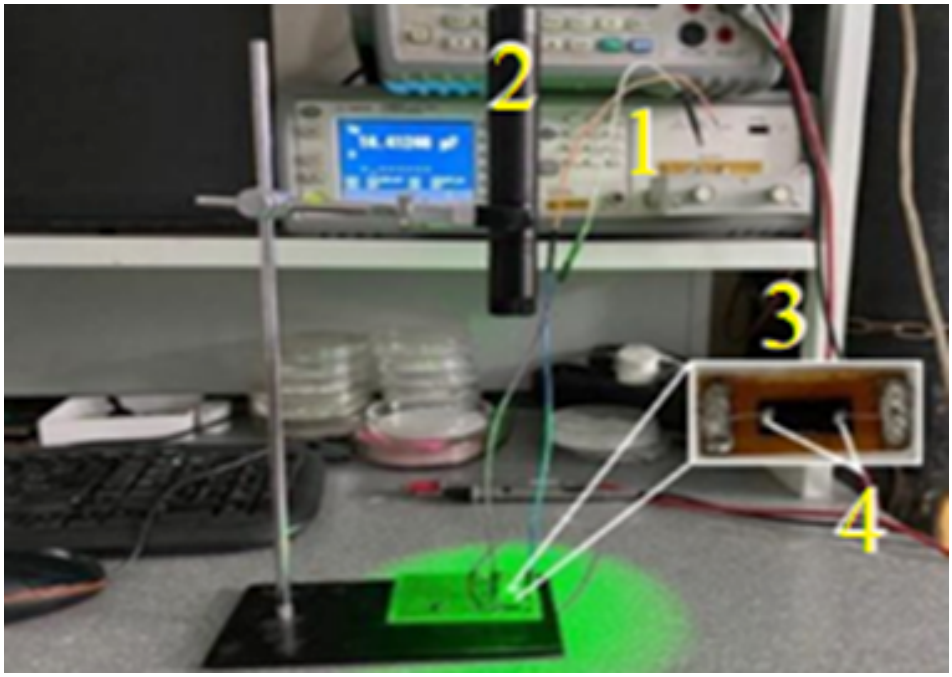

Figure 2 − Experimental setup: 1 − LCR meter the Agilent E4980A,
2 − infrared laser, 3 − a porous silicon film, 4 − metal contact

3 Experimental results and discussion

Figures 3 show the dependences of the electric current on the voltage of the VAC of porous silicon films with and without exposure to infrared laser radiation. In the range from -3 V to 3 V (figure 3(a)) – in natural light, from -2 V to 2 V (figure 3(b)) – when exposed to a laser, the VAC curves are characterized by the presence of oscillation, negative differential resistance, and hysteresis.

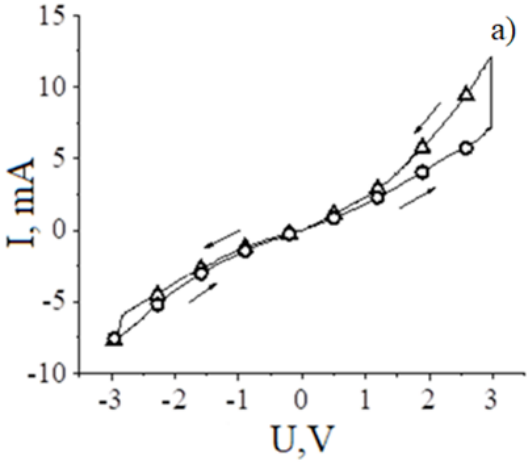

Figure 3 (a) − The volt-ampere characteristics of porous silicon in natural light.
Δ – for direct measurement,
○ − for reverse measurement

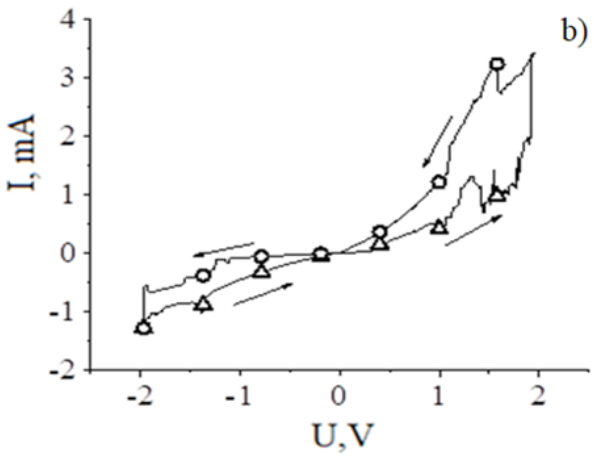

Figure 3 (b) − The volt-ampere characteristics of porous silicon when exposed to a laser.
Δ – for direct measurement,
○ – for reverse measurement

The nonlinear behavior of the VAC is typical, which can be explained by the dependence on the voltage of potential barriers in the structure of nanocrystal silicon. The experimental graph is characterized by the asymmetry of the hysteresis loops at forward and reverse (U<0) currents. The reverse current is significantly (~3 times) less than the forward current (U>0) under laser illumination. In this case, the current switching peaks are observed. Without laser action, current surges are not observed.

The difference in the shape of the curves during repeated transmission of current through the film indicates a change in its structure and the presence of memristive properties of the film.

Figure 4 shows the volt-farad characteristics of a porous silicon sample obtained at different frequencies (f) of the external voltage U (f) under the influence of a laser and in natural light.

The volt-farad characteristics in the form of hysteresis are obtained when the voltage increases from 0 V to 2 V, and then when it decreases. In natural light, the capacitance value decreases and stabilizes as the voltage increases. In natural light, a sample of porous silicon has properties similar to the metal-dielectric-semiconductor structure [22]. When a laser beam is applied to a porous silicon sample, the electrical capacity at a constant charge is inversely proportional to the voltage. The energy of the laser beam increases the energy of additional charge carriers in the valence band to the level of the conduction band, which increases the capacitance value. In figure 4 (a), when illuminated by a laser beam, a negative capacitance value is observed, with a low voltage value. As noted in [20], negative capacitance occurs due to a monotonous transient process with a small change in voltage, i.e., due to a decrease in charge.

Figure 5 shows the volt-farad characteristics of a porous silicon sample in natural light, under laser and incandescent illumination at a voltage frequency of 100 kHz.

Table 1 shows the areas of the hysteresis curves of the volt-farad characteristics obtained under different lighting conditions in conventional units. The area of the hysteresis curves obtained by laser and lamp illumination of the film increases by 2.54 and 1.87 times. When simultaneously illuminated with a laser and a lamp, an increase in the area of 4.5 times is observed.

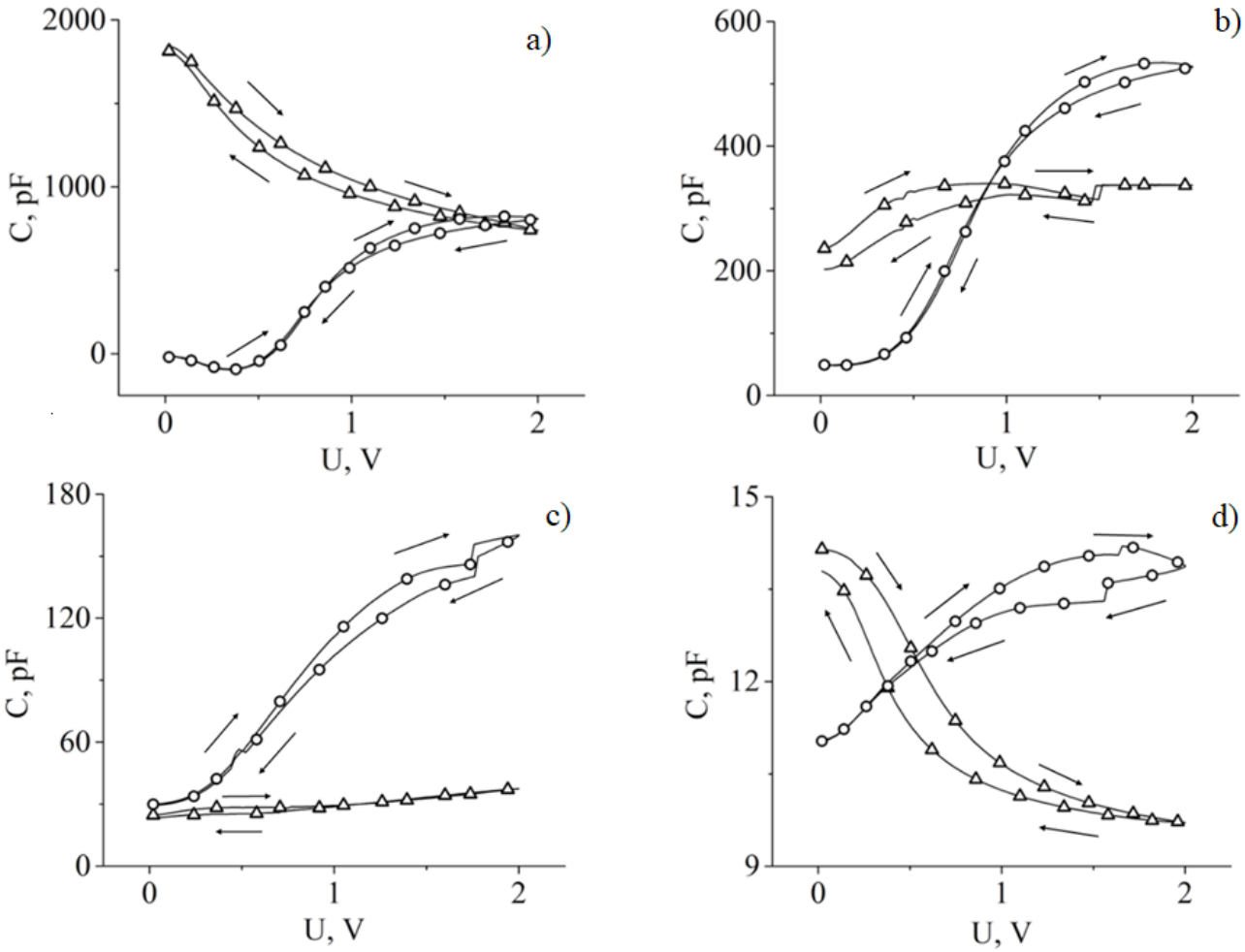

Figure 4 − The volt-farad characteristics of a porous silicon sample, frequency f (kHz):
(a) − 1, (b) −10, (c) − 10^2; (d) −10^3
Δ − in natural light conditions; ○ − when illuminated by a laser beam

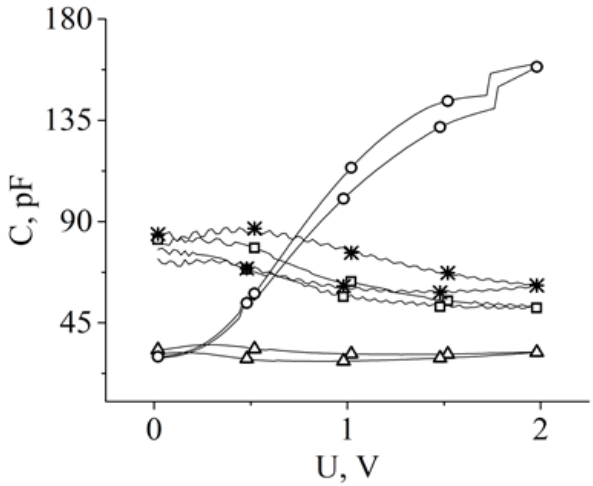

Figure 5 − The volt-farad characteristics
of porous silicon samples: Δ – in natural light,
○ − under laser illumination, □ – under illumination

Table 1 – Changes in the hysteresis characteristics under different illumination of the nanofilm. S_0 is a value of S in natural light

Type of lighting	Conditional hysteresis area (S)	S_x / S_0
Natural	5.23	-
Laser	13.33	2.54
Lamp	9.78	1.87
Laser+lamp	23.55	4.5

Figure 6 shows the change in the volt-farad characteristic when a voltage is applied from 0 V to 2 V, at a voltage frequency that coincides with the characteristic size of the nanofilm (~10^{-3}m) and the propagation speed of the electromagnetic wave (~10^8m/s). The resonant decrease in the capacitance (~10^5Hz) is observed.

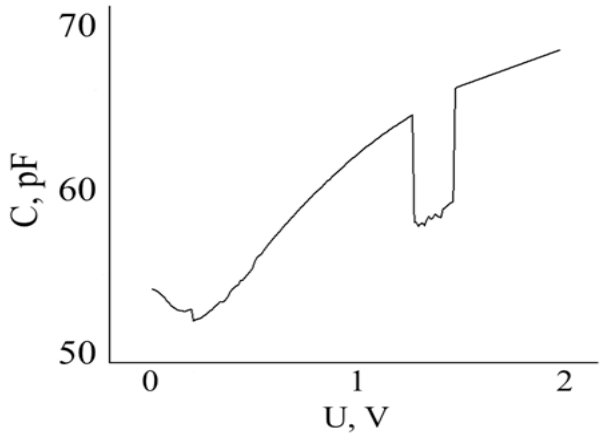

Figure 6 − The volt-farad characteristic of a porous silicon sample at 100 kHz

There is an abrupt decrease in the capacitance in the voltage range 1.2-1.4 V, comparable to the value of the width of the energy-forbidden zone of silicon. A sharp decrease in the capacitance value is associated with a decrease in the charge when the voltage is resonant.

Figure 7 shows the dependence of capacitance on the frequency at a constant voltage value.

As the frequency increases, the capacitance value decreases. This means that porous silicon structures have depletion and charge accumulation zones, as in metal-dielectric-semiconductor devices.

At low frequencies, the capacitance value is higher, since the conditions of the boundary loop are in equilibrium. At high frequencies, the capacitance is related to the spatial distribution of charges, and the boundary conditions of the loops are not affected by the voltage [22]. A similar result was obtained in [19, 21, 22].

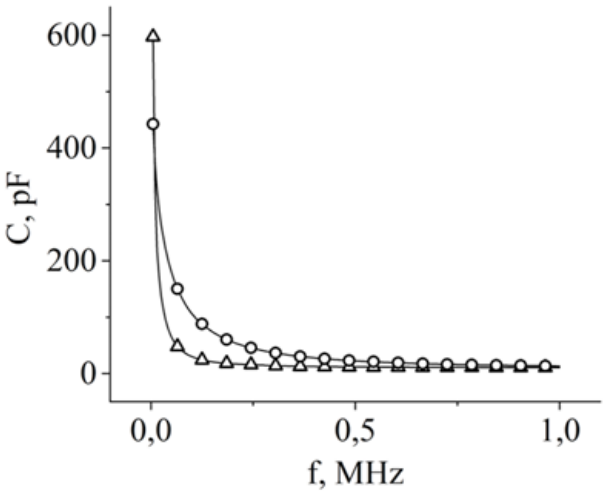

Figure 7 – The frequency dependence of the capacitance at a constant voltage U = 1 V, Δ − in natural light; ○ − in laser light

4. Conclusion

The various qualitative and quantitative changes in the electrical conductivity and electrical capacity of nanoporous semiconductor films are shown experimentally. Some general regularities are established: non-linear, hysteresis dependence of electric current, electric capacity on voltage both in natural light and under laser radiation. In the latter case, the characteristics increase up to 3-4 times. The appearance of chaotic bursts jumps in changes in electric current and capacitance is observed at external voltage values close to the value of the energy band gap of the semiconductor. As the process repeats, the structure of the nanofilm changes: the conductivity increases, and the resistance decreases. These phenomena of current switching and memristor behavior of the capacitance can also be realized on spatial scales of the order of a micron, as resonant effects of the characteristic frequencies of the film and external perturbation.

The established experimental facts can serve as a basis for improving the nanotechnology of memory elements, sensors, photo converters, and for building the necessary physical theories.

References

1. Praveenkumar S., Lingaraja D., Mathi P.M., Ram G.D. An experimental study of optoelectronic properties of porous silicon for solar cell application // Optik. -2018. –Vol. 178. –P. 216-223.

2. Bisi O., Ossicini S., Pavesi L. Porous silicon: a quantum sponge structure for silicon based optoelectronics // Surface Science Reports. -2000. –Vol. 38. –P. 1–126.

3. Skelton J.M., Pallipurath A.R., Lee T.-H., Elliott S.R. Atomistic origin of the enhanced crystallization speed and n-type conductivity in Bi-doped Ge-Sb-Te phase-change materials // Advanced Functional Materials. -2014. –Vol. 24. –No. 46. –P. 7291-7300.

4. Wang B., Qiu J., Feng H., Sakai E., Komiyama T. KOH-activated nitrogen doped porous carbon nanowires with superior performance in supercapacitors // Electrochimica Acta. -2016. –Vol. 190. –P. 229–239.

5. Ibraimov M.K., Sagidolda Y., Rumyantsev S.L., Zhanabaev Z.Zh., Shur M.S. Selective gas sensor using porous silicon // Sensor letters. -2016. –Vol.14. –No.6. –P. 588-591.

6. Bennett M.F., Bittner Z.S., Forbes D.V., Tatavarti S.R., Ahrenkiel S. P., Wibowo A., Pan N., Chern K., Hubbard S.M. Epitaxial lift-off of quantum dot enhanced GaAs single junction solar cells // Appl. Phys. Lett. -2013. –Vol. 103. –No.21. –P. 213902.

7. Ge D., Shi J., Wei J., Zhang L., Zhang Z. Optical sensing analysis of bilayer porous silicon nanostructure // Journal of Physics and Chemistry of Solids. -2019. –Vol. 130. –P. 217-221.

8. Chakrabarty S., Mandal S., Ghanta U., Das J., Hossain S.M. Current controlled switching in Si/PS/a-Si heterostructure // Materials Today: Proceedings. – 2018. – Vol. 5. – No. 3. – P. 9790-9797.

9. Nam Do V., Dollfus P. Negative differential resistance in zigzag-edge graphene nanoribbon junctions // Journal of Applied Physics. -2010. –Vol. 107. –No. 6. –P. 063705.

10. Chen K.H., Fang Y.K., Shieh K.H., Liou W.R. Preparation and analysis of the negative resistance characteristic in an amorphous silicon and silicon–carbide single-barrier device // Applied physics letters. -1994. –Vol. 65. –No. 22. –P. 2815-2817.

11. Yu L.W., Chen K.J., Song J., Wang J.M., Xu J., Li W., Huang X.F. Coulomb blockade induced negative differential resistance effect in a self-assembly Si quantum dots array at room temperature // Thin Solid Films. -2007. –Vol. 515. –No. 13, -P. 5466-5470.

12. Lee M.K., Chu C.H., Tseng Y.C., Shyr J.M., Kao C.H. Negative differential resistance of porous silicon // IEEE Electron Device Letters. -2000. –Vol. 21. –No. 12. –P. 587-589.

13. Marin O. et al. Negative differential resistance in porous silicon devices at room temperature // Superlattices and Microstructures. -2015. –Vol. 79. –P. 45-53.

14. Martínez L., Becerra D., Agarwal V. Dual layer ZnO configuration over nanostructured porous silicon substrate for enhanced memristive switching // Superlattices and Microstructures. -2016. –Vol. 100. –P. 89-96.

15. Lee M. K. et al. Negative differential resistance of porous silicon // IEEE Electron Device Letters. -2000. –Vol. 21. –No. 12. –P. 587-589.

16. Betty C. A. Highly sensitive capacitive immunosensor based on porous silicon–polyaniline structure: Bias dependence on specificity // Biosensors and Bioelectronics. -2009. –Vol. 25. –No. 2. -P. 338-343.

17. Mkhitaryan Z. H. et al. I–V characteristics of structures with porous silicon in electrolyte // Optical Materials. -2005. –Vol. 27. –No.5. –P. 962-966.

18. Ocampo O., Antúnez E. E., Agarwal V. Memristive devices from porous silicon–ZnO/VO_2 nanocomposites // Superlattices and Microstructures. -2015. –Vol. 88. –P. 198-203.

19. Garzon-Roman A., Milosevic O., Rabanal M. E. Morphological, structural, and functional properties of vertically aligned carbon nanotubes deposited on porous silicon layers by ultrasonic spray pyrolysis // Microporous and Mesoporous Materials. -2020. –Vol. 292. –P. 109738.

20. Sancho A., Arizti F., Gracia F. J. Porous silicon for the development of capacitive microstructures // Microelectronic engineering. -2009. –Vol. 86. –No.11. –P. 2144-2148.

21. Kaur R., Arora A., Tripathi S. K. Fabrication and characterization of metal insulator semiconductor Ag/PVA/GO/PVA/n-Si/Ag device // Microelectronic Engineering. -2020. –Vol. 233. –P. 111419.

22. Gabouze N., Belhousse S., Cheraga H., Ghellai N., Ouadah Y., Belkacem Y., Keffous A. CO_2 and H_2 detection with a CH_x/porous silicon-based sensor // Vacuum. -2006. –Vol. 80(9). –P. 986-989.

IRSTI 28.23.37 https://doi.org/10.26577/phst.2020.v7.i2.07

Methods of the development of the architecture of the neural networks for identification and authentication of individuals

O. Y. Golikov* and M. A. Ramos

Laboratory of Low Temperatures, Department of Condensed Matter Physics,
Condensed Matter Physics Center (IFIMAC) and Nicolás Cabrera Institute,
Autonomous University of Madrid, 7, Francisco Tomás y Valiente, 28049 Madrid, Spain
*e-mail:golikov.ua@gmail.com

This paper deals with the neural network methods of the implementation of systems of identification of individuals based on videos and photographs. Over the last few decades, it has been considered to be one of the most powerful tools and has become very popular in the literature as it is able to handle a huge amount of data. The neural network architectures used in modern biometric identification systems have been reviewed. Based on the research conducted in this field, an approach was developed that can improve the accuracy of object recognition in photo and video images by increasing the quality of the attributes of the weights and reducing the number of the weights, as well as the number of the connections. The basis of the developed neural network model is a multilayer perceptron; the main system is a convolutional neural network. The neural network model has been implemented using the Python programming language with the most popular machine learning libraries Keras and TensorFlow. In addition, we will also enumerate the parameters that affect CNN efficiency.

Key words: biometric identification of individuals, three-dimensional object recognition, convolutional neural network, deep machine learning, subsampling.
PACS numbers: 84.35.+i, 87.18.Sn, 07.05.Mh

1 Introduction

Since the 1990s, systems based on machine learning methods and annotated database information have been widely used for automatic information recognition [1, 2, 3, 4]. By today, the field of "character and pattern recognition" has become very popular among researchers due to the possibility of increasingly frequent application of the technology in daily human activities. The most prominent examples of the use of information recognition technology are the recognition of faces, speech, images, handwritten documents, number plates, barcodes. The recognition of faces, speech and handwritten input is of particular interest among these examples as these parameters can solve one of the most topical problems of the modern digital society: identification and authentication of individuals [2, 3, 5]. Through the application of automatic recognition, it is possible to achieve digital "computer-based" identification of a person, which, in turn, would contribute to the replacement of the current, already obsolete methods.

The development of high-speed computing machinery, the increased performance of modern computers and improvements in audio and video capture systems indicate that further advancements in machine learning and autonomous object recognition technology are appropriate and that such technology should be introduced even more widely into everyday life.

Researchers have written a large number of publications on the problem of object recognition and the identification of individuals, but despite this, this topic is still relevant. This is primarily due to the large volume of information and the uncertainty that are inherent to the recognition technology and the objects, respectively, as well as to the improvement of computing technology capabilities.

Most modern biometric recognition systems based on the unique biological characteristics of an individual have two major drawbacks, which make the use of neural networks and video even more sensible [6, 7]:

– the use of special and/or expensive equipment;

– physical contact with the devices used for identification (fingerprinting, iris scanning).

Thus, the use of face recognition methods based on the neural networks for identity verification helps to create a fairly efficient, yet inexpensive and easy to implement solution to this problem [8].

A priority direction in the field of image detection and recognition in photo and video today is the use of Convolutional Neural Networks (CNN) [9, 10, 11, 12]. The main advantage of this method of neural network implementation is that the algorithm itself extracts information attributes, relative to which the weights are calculated [12].

The aim of this research is to investigate modern identification methods and to improve the quality of image recognition. The scientific value lies in the creation of a more efficient image analyser based on the already existing neural network organisation approaches, without using "heavy" methods. Such methods involve software tools that spend too many resources in the process of recognition (neural networks with pixel-by-pixel comparison) [13]. The practical value lies in the possibility of applying this method of neural network organisation as a working system for the identification of individuals (e.g., in the banking, government, law enforcement sectors).

2 Neural Network Model Architecture and Its Training.

Convolutional neural networks are a class of neural network models that originated from the studies of the feline visual apparatus conducted by Hubel and Wiesel in the 1960s [14]. The result of these studies was the discovery of two types of neurons responsible for the visual perception of animals: the first type has the properties of local sensitivity and is responsible for detecting the simplest characteristics of objects (approximate silhouette, extreme points and angles of an object); the second type facilitates the recognition of higher-level features of objects, using combinations of neurons of the first type.

The first real-world model that implemented the detected behaviour of feline visual neurons was the neocognitron of Fukushima [15]. It was created using supervised training of a linear classifier and unsupervised adjustment of the filter bank. Subsequent research in this area made the complete transition to the supervised form of training possible and also greatly simplified the architecture of the neural network. Eventually, a new convolutional structure was developed, which is currently gaining more and more forms of practical application: navigation systems, image recognition, identification of individuals, recovery of noisy signals and much more [16].

There are several architectures of convolutional neural networks developed so far, which differ from each other in the topology of layers, the way the learning process is organised, activation function, etc. One of the classic architectures of convolutional neural networks is the LeNet-5 neural network model developed by Yan LeCun in the late 1990s [17].

Fig. 1 shows a schematic diagram of a classical, multilayer, fully connected neural network and how it works. Classic multilayer neural networks have two significant disadvantages that arise directly from the network architecture because the inter-neuronal connections between layers are organized by means of "each to each" connection.

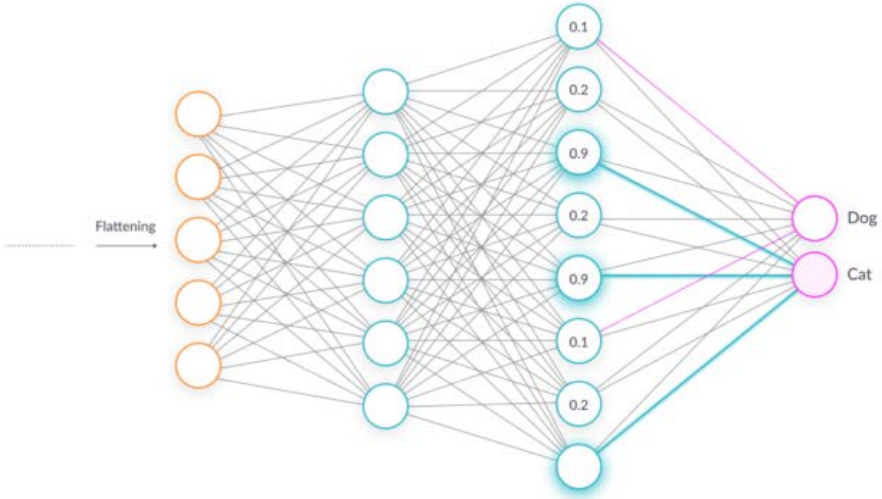

Figure 1 – Fully-connected layer

Because of this kind of connection, the image has the appearance of an n-dimensional vector, which does not take into account the local two-dimensional organisation of the pixels and the possibility of image deformation. At the same time, the convolutional neural network architecture (Fig. 2) provides an opportunity to correct the shortcomings of the classical multilayer neural network. It implements the principles of the neocognitron architecture, which is simplified and augmented with an error backpropagation algorithm used for training [18, 19].

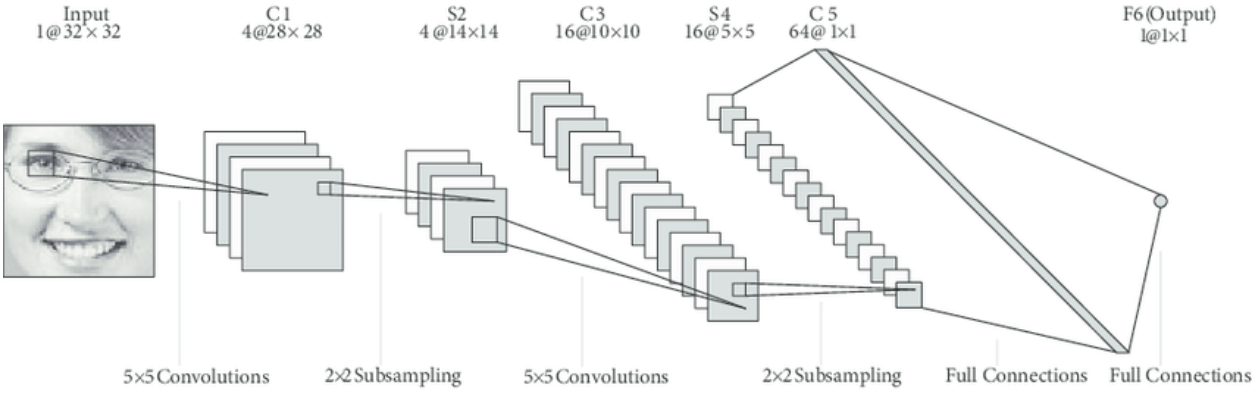

Figure 2 – LeNet introduced by Yan LeCun [17]

The use of local receptor fields, weights and hierarchical organisation with spatial subsamples in convolutional neural networks enables local two-dimensional connectivity of the neurons and detection of individual facial features that can be located anywhere in an image [20].

A convolutional neural network is able to provide partial robustness to changes in image scale, displacements, rotations, changes in viewing angle and other types of distortions. As already mentioned, a convolutional neural network architecture is multi-layered, but it can be divided into two main types: Convolutional and Subsampling, which alternate with each other in architectures. Each individual layer contains multiple planes. Neurons from any of the planes have identical weights that come to all the local fragments of the previous layer (identical to the human visual cortex). The incoming information is "scanned" by a window of a certain, often small, size; information is then "weighed" by a set of weights, and the result of these operations is transmitted to the corresponding neuron of the subsequent layer. Such planes are called feature maps. Each of the feature maps selects certain parts of the input image, sending the result to the next subsampling layer. The subsampling layer reduces the scale of the planes through the local averaging of the weights, thereby organising the hierarchical structure of the convolutional neural network. This algorithm corresponds to the first type of neurons in the feline visual apparatus mentioned above. Subsequent layers corresponding to the second type of neuron extract more general characteristics from images, which are less dependent on distortion [18].

A comparison of multilayer neural networks with convolutional neural networks has shown a significant advantage of the latter both in terms of learning speed and quality of object recognition. At present, the parameters of learning speed, performance and percentage of accurate recognition play a key role in the development of the image recognition systems (including human identification systems).

3 Algorithm for Selecting a Convolutional Neural Network Architecture.

Before starting to implement the algorithm, it is necessary to introduce the concept of partial partitioning, which means the set of convolutional neural network layers $N = \{N_1, N_2, \dots, N_i\}$, where i is the number of neural network layers determined experimentally. The idea of introducing the following algorithm is to enumerate a combinatorial set of different configurations that are constrained by certain parameters and layout rules. In order to reduce the enumeration space and cut off the futile alternatives, we will rely on the following conclusion:

If from the architecture of the convolutional neural network $N^1 = N_1^1, N_2^1, \dots, N_i^1$ the recognition

accuracy P^1 was obtained after its training, then architecture $N^2 = N_1^2, N_2^2, \dots, N_i^2$ can be obtained by changing parameter a_j in one of the layers $N_x^1 = k_x^1 a_j$ to parameter a_{j+1} $N_x^2 = k_x^2 a_{j+1}$, where $x \in [1, \dots, i]$, k_x is the number of elements in the word with recognition accuracy $P^2 < P^1$, then for neural network architecture $N^3 = N_1^3, N_2^3, \dots, N_i^3$ c $N_x^3 = (k_x^2+1)a_{j+1}$, the recognition accuracy will be even lower $P^3 < P^2 < P^1$ and further training of this branch is not needed.

The layout algorithm of the convolutional neural network architecture can be described as follows:

1. The input and the output layers of the desired architecture are created based on the data used as a basis:

$$- x_{i,j}^1 = m * n * ch;$$

$$- y_{i,j}^1 = r.$$

2. A randomly chosen number of layers i is set, and the layout counter is set to $j = 1$. A set A of convolutional neural networks is found.

3. $Q^* = 0$, $M^* = 0$, $N, N_1, \dots, Z_1 = \emptyset, j = j + 1$, $A = \emptyset$ is a set of futile architectures.

4. $n = 1$ is the layer counter.

5. $k = 1$ is the counter of neurons in the layer.

6. Check if the condition $n < i$ (the current layer is not the last one) is met. If the condition is true, proceed to the next step, otherwise, proceed to step 13.

7. Assign γ^5 as a rule of selecting the candidate a_i from the set of all neural network architectures A.

8. According to the rule γ^5, element a_k is selected and placed in N_1,

9. The number of inter-neuronal connections is found:

$$Q_k^* = \sum W_{a_k} x_{l,j}^i, Q^* = Q^* + Q_k^*,$$

and the number of weights used:

$$M_k^* = W_{a_k} x_{l,j}^i, M^* = M^* + M_k^*.$$

10. Check if the condition $Q^* \le \frac{Q}{l}$ is met. If the condition is true, increment $k = k + 1$ and return to step 6. If the condition is false, increment $n = n + 1$ and return to step 5.

11. Insert i fully-connected output neurons in the subset N_1, $N = \{N_1, \dots, N_i\}$.

12. Check if the cut-off condition is met by the model. If the condition is true, then $N = \{N_1, \dots, N_i\}$ is placed in A. If the condition is false, proceed to the next step.

13. Model $N = \{N_1, \dots, N_i\}$ is excluded from the set of all convolutional neural networks A. After this model is trained on the test dataset, it is added to the database along with the result of the training P, P_1, P_2 under the name A^j.

14. Untested alternatives of the set of neural networks A are checked. If untested architectures exist, return to step 3, otherwise, proceed to the next step.

15. Selection of the architecture with the maximum $P - max$ value from the database A^j.

4 Results of the Experiment.

The training data set for the experiment consisted of photographs of real people. The architecture of the convolutional neural network was obtained by using the algorithm proposed above. The sizes of the filter windows were 3x3, 7x7, 11x11; the subsampling window size was 2x2; the activation function was adam (adaptive moment estimation) [21].

The important point was the comparison of the parameters such as epoch accuracy and epoch loss during the training of the neural networks. Figure 3 and Figure 4 show the comparison of these parameters for neural networks with different filter window and different volume of the training base.

The graphs show that with a 3x3 filter window size, high accuracy is achieved faster than with the 7x7 and 11x11 windows. At the same time, the training of the neural network with a 3x3 window is faster. A similar pattern can be observed in the case of epoch loss.

It is worth noting that after certain epochs of training in some cases epoch loss increases along with a decrease in epoch accuracy. Thus, there is a question of whether it is reasonable to use a large number of epochs, which can lead to the deterioration of the neural network parameters.

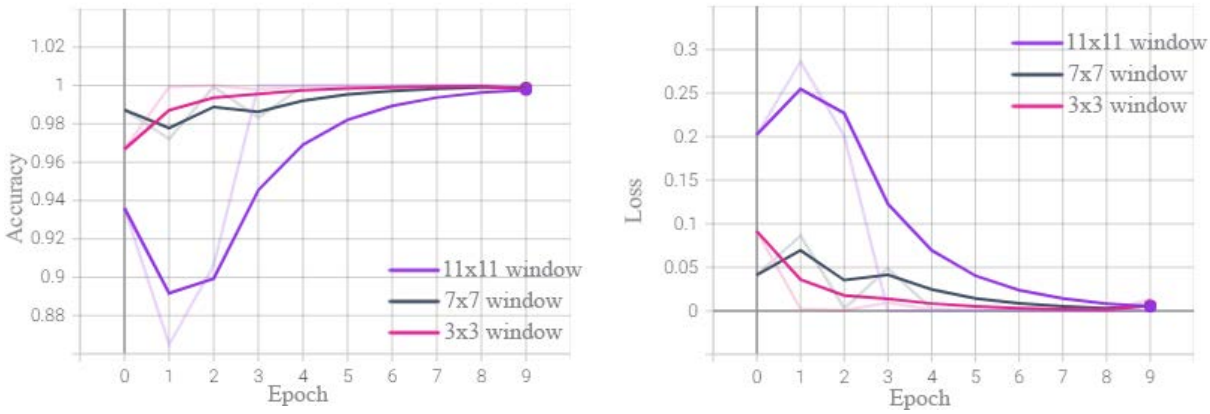

Figure 3 – The dependency of epoch accuracy and epoch loss on the size of the filter window when training data equals 20000

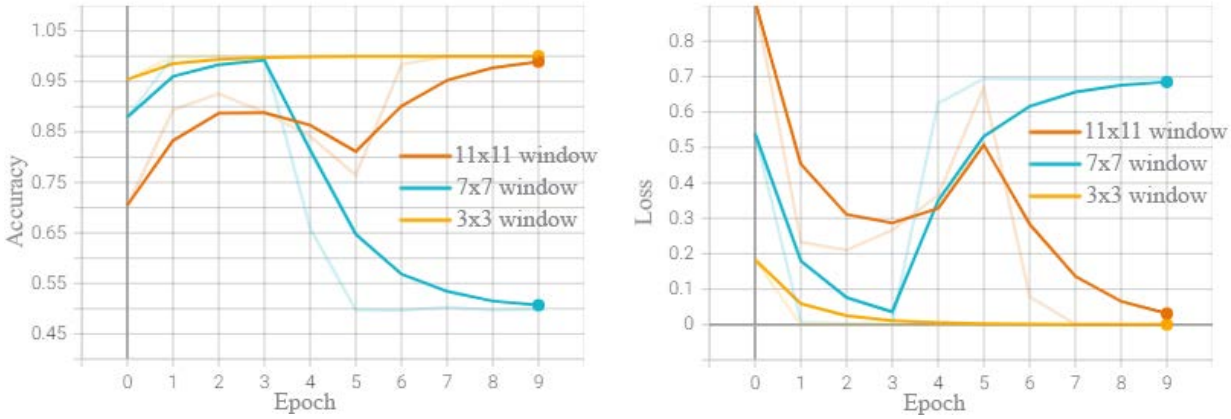

Figure 4 – The dependency of epoch accuracy and epoch loss on the size of the filter window when training data equals 4000

5 Conclusion

In this paper, methods of selection of the appropriate neural network architecture were reviewed, using the proposed algorithm. By varying the size of the filter window, the dependencies that affect the process of training, as well as the quality of the initial neural network, were obtained. The obtained data provides food for thought on how to properly constrain the process of training of a neural network in order to achieve an optimal solution with respect to the duration of the training and the quality of recognition. The deterioration of the parameters after a certain epoch of training requires further explanation as well. It is possible that this phenomenon is caused by the activation function reaching one of the local minima.

References

1 Burshtein D., Robust parametric modeling of durations in hidden Markov models // IEEE Transactions on Speech and Audio Processing, May 1996. – 1996. – Vol. 1. – No. 3. – P. 240-242.

2 Gunawardana A., Mahajan M., Acero A., Platt J. C. Hidden conditional random fields for phone classification // In Proceedings Interspeech. – 2005. – P. 1117–1120.

3 Bourlard H., Wellekens C.J. Links between Markov models and multilayer perceptrons // IEEE Transactions on Pattern Analysis and Machine Intelligence. – 1990. – Vol. 12. – No. 12. – P. 1167-1178.

4 Nefian A.V., Liang L.H., Pi X., Xiaoxiang X., Mao C., Murphy K. A coupled HMM for audio-visual speech recognition // In Proceedings International Conference ICASSP-2002, Orlando, USA. – 2002. – P. 2013–2016.

5 Jain A.K., Bolle R., Pankanti S., eds., Biometrics: Personal Identification in networked society, Kluwer Academic, Norwell, Mass., 1999, 410 p.

6 Pankanti Sh., Bolle R.M. Antil Jain. Biometrics: The future of identification // IEEE Computer. – 2000. – P. 46-49.

7 Foltyniewicz R. Efficient high order neural network for rotation, translation and distance invariant recognition of gray scale images // Lecture Notes in Computer Science - Computer Analysis of Images and Patterns. – 1995. – P. 424-431.

8 Turner R. E. Lecture 14: Convolutional neural networks for computer vision. – 2014. – P.1-30.

9 Dumoulin V., Visin F. A guide to convolution arithmetic for deep learning. – 2016. – P. 1–28.

10 Kokkinos I., Paris E. C., Group G. Introduction to deep learning convolutional networks. Dropout, Maxout 1. – P. 1–70.

11 Andrew Lavin, Scott Gray; Proceedings of the IEEE Conference on Computer Vision and Pattern Recognition (CVPR). – 2016. – P. 4013-4021.

12 Sarıgül M., Ozyildirim B.M., Avci M., Differential convolutional neural network // Neural Networks. – 2019. – Vol. 116. – P. 279-287.

13 Salu Y., Tilton J. Classification of multispectral image data by the binary diamond neural network and by nonparametric, pixel-by-pixel methods // IEEE Transactions on Geoscience and Remote Sensing. – 1993. – Vol. 31. – No. 3. – P. 606-617.

14 Hubel D.H., Wiesel T.N. Receptive fields, binocular interaction and functional architecture in the cat's visual cortex // Journal of Physiology London. – 1962. – Vol. 15. – P 106–154.

15 Fukushima K., Miyake S., Ito T. Neocognitron: A neural network model for a mechanism of visual pattern recognition // IEEE Transactions on Systems, Man, and Cybernetics, – 1983. – Vol. SMC-13. – No. 5. – P. 826-834.

16 LeCun Y., Kavukvuoglu K., Farabet C. Convolutional networks and applications in vision // Proc. IEEE Int. Symposium on Circuits and Systems. – 2010. – P 253–256.

17 LeCun, Y., Bottou, L., Bengio, Y. and Haffner, P. Gradientbased learning applied to document recognition // Proceedings of the IEEE -1990. –Vol. 86(11). – P.2278-2324.

18 Lawrence S., Giles C. L., Tsoi A. C., Back A. D. Face recognition: A convolutional neural network approach // IEEE Transact. on Neural Networks, Special Issue on Neural Networks and Pattern Recognition. – 1997. – P. 1-24.

19 Santaji G., Jayshree G., Shamla M., Dhanaji G. Neural networks for facerecognition using SOM // IJCST. -2010. – Vol. 1, – No. 2. – P. 65—67.

20 Albawi S., Mohammed T. A., Al-Zawi S. Understanding of a convolutional neural network // 2017 International Conference on Engineering and Technology (ICET). – P. 1-6

21 Kingma D.P., Ba J.L., Adam: A method for stochastic optimization // ICLR. – 2015. – P 58–62.

CONTENTS